JCB Journal of Cell Biology

ARTICLE

LRR1-mediated replisome disassembly promotes DNA replication by recycling replisome components

Yilin Fan[1,2], Marielle S. Köberlin[1], Nalin Ratnayeke[1,2], Chad Liu[1], Madhura Deshpande[3], Jeannine Gerhardt[3,4], and Tobias Meyer[1,2]

After two converging DNA replication forks meet, active replisomes are disassembled and unloaded from chromatin. A key process in replisome disassembly is the unloading of CMG helicases (CDC45–MCM–GINS), which is initiated in *Caenorhabditis elegans* and *Xenopus laevis* by the E3 ubiquitin ligase CRL2^{LRR1}. Here, we show that human cells lacking LRR1 fail to unload CMG helicases and accumulate increasing amounts of chromatin-bound replisome components as cells progress through S phase. Markedly, we demonstrate that the failure to disassemble replisomes reduces the rate of DNA replication increasingly throughout S phase by sequestering rate-limiting replisome components on chromatin and blocking their recycling. Continued binding of CMG helicases to chromatin during G2 phase blocks mitosis by activating an ATR-mediated G2/M checkpoint. Finally, we provide evidence that *LRR1* is an essential gene for human cell division, suggesting that CRL2^{LRR1} enzyme activity is required for the proliferation of cancer cells and is thus a potential target for cancer therapy.

Introduction

DNA replication occurs during S phase and is a highly orchestrated process consisting of initiation, elongation, and termination steps. Defects in these processes frequently lead to genome instability and loss of cell viability (Bell and Labib, 2016). During initiation, DNA is licensed at the end of mitosis and in G1 phase when heterohexamer rings of MCM2–7 are recruited to origins of replication. During S phase, licensed origins are fired when CDC45, the four-subunit GINS1–4 complex, and other factors bind to MCM2–7, forming an active CDC45–MCM–GINS (CMG) DNA helicase (Bell and Labib, 2016; Costa et al., 2013). During elongation, the CMG helicase travels at the front of the replication fork and unwinds parental double-stranded DNA, while other protein complexes in the replisome perform the various steps of DNA synthesis (Burgers and Kunkel, 2017; Johansson and Dixon, 2013).

After two opposing forks complete replication of the replicon and converge, CMG helicases are removed from DNA in a two-step process (Dewar and Walter, 2017): CMGs are polyubiquitylated on MCM7 (Deegan et al., 2020; Low et al., 2020; Maric et al., 2014; Moreno et al., 2014) and subsequently extracted from DNA by the ATPase p97 (also known as CDC48 or VCP; Franz et al., 2011; Maric et al., 2014; Moreno et al., 2014), leading to the disassembly of the entire replisome (Dewar et al., 2015; Dewar et al., 2017; Sonneville et al., 2017). The E3 ubiquitin ligase responsible for MCM7 polyubiquitylation is SCF^{Dia2} in *Saccharomyces cerevisiae* (Maric et al., 2014) and CRL2^{LRR1} in *Caenorhabditis elegans* and *Xenopus laevis* (Dewar et al., 2017; Sonneville et al., 2017).

While replisome disassembly has been mechanistically studied in yeast, worms, and frogs, it is unclear how the system works in human cells. Genetic loss of *lrr-1* in worms results in mitotic block in the early embryo and germ line (Burger et al., 2013; Merlet et al., 2010). In contrast, inhibition of CRL2^{LRR1} activity in frog egg extracts does not block mitotic entry (Priego Moreno et al., 2019). This raises the question whether the *LRR1* gene is generally required for cell division. Furthermore, there is an alternative, LRR1-independent mechanism in worms and frogs that disassembles replisomes during mitosis (Deng et al., 2019; Priego Moreno et al., 2019; Sonneville et al., 2019; Sonneville et al., 2017). The presence of two replisome disassembly pathways poses the question whether the LRR1-dependent pathway is required for proper progression through S phase. Importantly for this study, it was not known whether the homologue human *LRR1* gene mediates CMG unloading, whether *LRR1* is an essential gene for human cell division, and whether LRR1-mediated replisome disassembly is required for S-phase progression in human cells.

Eukaryotic cells employ multiple layers of control to ensure that DNA replication is tightly coordinated with other cell-cycle

[1]Department of Chemical and Systems Biology, Stanford University School of Medicine, Stanford, CA; [2]Department of Cell and Developmental Biology, Weill Cornell Medicine, New York, NY; [3]Ronald O. Perelman and Claudia Cohen Center for Reproductive Medicine, Weill Cornell Medicine, New York, NY; [4]Department of Obstetrics and Gynecology, Weill Cornell Medicine, New York, NY.

Correspondence to Tobias Meyer: tom4003@med.cornell.edu; C. Liu's present address is Department of Discovery Oncology, Genentech, Inc., South San Francisco, CA.

events, including a cell cycle–specific transcription program that has to be induced before DNA replication starts (Costa et al., 2013; Limas and Cook, 2019). In mammalian cells, the majority of proteins involved in DNA replication initiation and elongation are encoded by target genes of the E2F transcription factors (Bracken et al., 2004; Burgers and Kunkel, 2017; Costa et al., 2013; Dimova and Dyson, 2005). E2F activity is repressed when bound by the retinoblastoma protein (Rb), and the repression is relieved when Rb is hyperphosphorylated at ∼15 sites by cyclin-dependent kinases (CDK) CDK4/6 and CDK2 (Fig. 1 A; Dimova and Dyson, 2005; Malumbres and Barbacid, 2001).

Our study was motivated by our identification of a set of 459 CDK4/6 activity-regulated human genes that includes many genes uniquely needed for DNA replication and mitosis. Through a targeted CRISPR screen of a subset of 30 poorly understood genes selected as potential regulators of S-phase progression, we identified LRR1 as a strong regulator of the global rate of DNA replication. We show that LRR1 is required for CMG unloading and replisome disassembly during S phase in human cells. Loss of LRR1 results in a gradual accumulation of chromatin-bound CMG helicases and other replisome components throughout S phase. Markedly, we demonstrate that failure to disassemble replisomes reduces the rate of DNA replication increasingly throughout S phase by sequestering rate-limiting replisome components on chromatin and blocking their recycling. During G2 phase, continued binding of CMG helicases to chromatin triggers an ATR–Chk1–Wee1-dependent G2/M checkpoint that blocks entry into mitosis. Consistent with defects in DNA replication and mitotic entry in the absence of LRR1, our own data and analysis of published CRISPR screen datasets show that *LRR1* is an essential gene in normal and cancerous human cells that are actively dividing, suggesting that inhibition of $CRL2^{LRR1}$ enzyme activity is a potential target for cancer therapy.

Results

Identification of LRR1 as a regulator of S-phase progression based on RNA sequencing (RNA-Seq) analysis and a targeted CRISPR screen

To identify potential novel regulators of S-phase progression, we performed an RNA-Seq time-course analysis of nontransformed human breast epithelial cells (MCF10A) released into the cell cycle from serum starvation in the presence of DMSO or the specific CDK4/6 inhibitor palbociclib (Fig. 1 B; see Table S1 for raw read counts). CDK4/6 inhibition arrests the majority of cells in early G1 (Liu et al., 2020) by preventing activation of the E2F transcriptional program and progression into S/G2 (Dimova and Dyson, 2005; Malumbres and Barbacid, 2001). Indeed, we found that reported E2F target genes (Bracken et al., 2004) were down-regulated when CDK4/6 was inhibited (Fig. 1, C and D; see Table S2 for results from differential expression analysis). To establish a set of genes whose expression is dependent on CDK4/6 activity, we filtered for genes that were up-regulated at least twofold (false discovery rate–adjusted P value < 0.1) in control versus CDK4/6–inhibited conditions at any one of the time points after release, which led to the identification of 459 CDK4/6–dependent genes (Fig. S1, A and B; see Table S3 for gene list).

As expected, gene ontology (GO) analysis of CDK4/6–dependent genes identified an enrichment of genes involved in cell-cycle processes, including DNA replication, DNA repair, chromosome organization, and cell division (Fig. S1 C). To explore the transcriptional regulation of CDK4/6–dependent genes, we analyzed publicly available chromatin immunoprecipitation sequencing (ChIP-Seq) datasets from the ENCODE project (ENCODE Project Consortium, 2012; Davis et al., 2018). CDK4/6–dependent genes are enriched for E2F1 targets (Fisher's exact test, odds ratio = 7.4, $P = 7.7 \times 10^{-80}$), FOXM1 targets (odds ratio = 12.5, $P = 1.6 \times 10^{-89}$), and MYBL2 targets (odds ratio = 15.6, $P = 3.3 \times 10^{-96}$; Fig. 1 E; see Table S4 for lists of target genes). Within the set of CDK4/6–dependent genes, expression of E2F1 targets were up-regulated earlier after serum release than FOXM1 and MYBL2 targets (Fig. S1 D). These results are consistent with a cell cycle–dependent transcriptional program that starts with E2F activation in G1 and is followed by activation of FOXM1 and MYBL2 toward the end of S phase (Dimova and Dyson, 2005; Fischer and Müller, 2017; Laoukili et al., 2005; Sadasivam et al., 2012; Wang et al., 2005).

We manually annotated the function of CDK4/6–dependent genes and found 162 genes without well-characterized cell-cycle functions (Fig. 1 F and Table S3). GO term analysis on these 162 genes failed to identify a significant over-representation of known processes (data not shown). Analysis of ENCODE ChIP-Seq datasets nevertheless revealed an enrichment in these genes for E2F1 targets (Fisher's exact test, odds ratio = 3.8, $P = 6.4 \times 10^{-12}$), FOXM1 targets (odds ratio = 5.4, $P = 2.4 \times 10^{-11}$), and MYBL2 targets (odds ratio = 5.8, $P = 3.0 \times 10^{-10}$).

Next, we studied the function of a subset of these 162 CDK4/6–dependent genes without well-characterized cell-cycle functions by focusing on genes that were induced strongly and/or early, which may suggest a role in regulating DNA replication. We performed a targeted CRISPR screen on 30 candidate genes (see Fig. S1 B for gene list), where we transfected synthetic small guide RNAs (sgRNAs) into MCF10A cells stably expressing Cas9. Then we performed quantitative image-based cytometry (Toledo et al., 2013) and measured the rate of DNA replication in single cells by pulse labeling with a nucleoside analogue 5-ethynyl-2′-deoxyuridine (EdU; Fig. 1 G). Strikingly, we found that LRR1 knockout resulted in the strongest suppression of DNA replication (Fig. 1 H and Fig. S1 E). We confirmed that LRR1 expression is dependent on CDK4/6 activity at both the mRNA and protein levels (Fig. 1, I and J) and the LRR1 promoter region is bound by E2F1 (Fig. 1 K). LRR1 is the substrate recognition subunit of the E3 ubiquitin ligase $CRL2^{LRR1}$, whose homologues in worms and frogs have been shown to unload CMG helicases from chromatin after the completion of DNA replication (Dewar et al., 2017; Sonneville et al., 2017). However, the finding of a reduced DNA replication rate was unexpected since it has been shown previously that LRR1 depletion does not affect progression of DNA replication in frog egg extracts (Dewar et al., 2017; Sonneville et al., 2017). In contrast, our data suggest that LRR1-mediated CMG helicase unloading may be continuously required in human cells for efficient DNA replication.

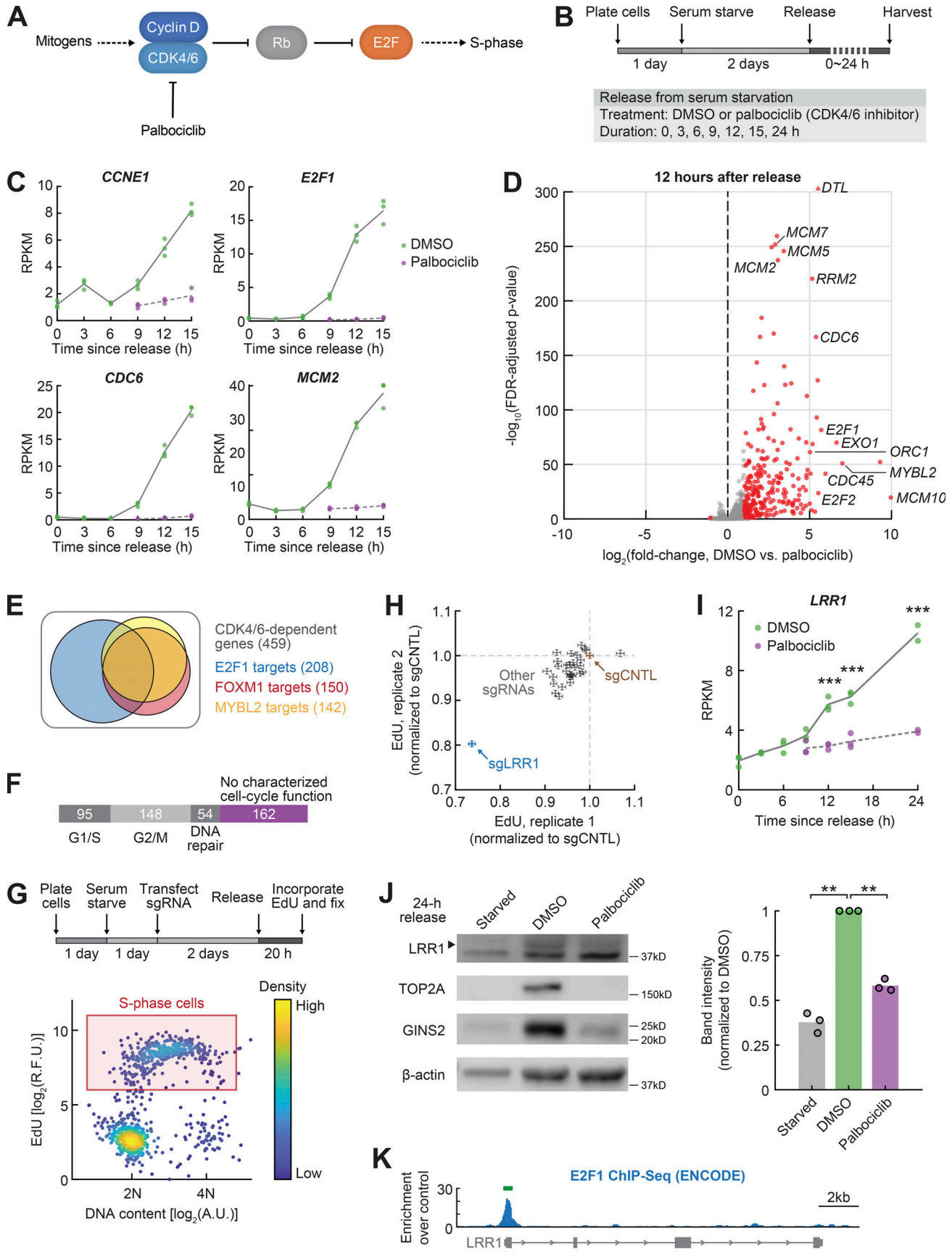

Figure 1. **Identification of LRR1 as a regulator of S-phase progression based on RNA-Seq analysis and a targeted CRISPR screen. (A)** Cell-cycle entry pathway in mammalian cells. Rb, retinoblastoma protein. **(B)** Schematic of experimental setup for RNA-Seq. **(C)** Examples of gene expression time course

measured by RNA-Seq. Each time point contains three independent experiments. RPKM, reads per kilobase of transcript per million mapped reads. **(D)** Volcano plot from differential expression analysis of three independent experiments. Differentially expressed genes ($|\log_2[\text{fold-change}]| > 1$, adjusted P value < 0.1) are highlighted. Labeled genes are examples of reported E2F targets (Bracken et al., 2004). FDR, false discovery rate. **(E)** Venn diagram of CDK4/6–dependent genes that are targets of E2F1, FOXM1, or MYBL2 (ENCODE ChIP-Seq datasets; see Materials and methods for details). **(F)** Manually annotated function of CDK4/6–dependent genes. **(G)** Top: Experimental setup. Bottom: Schematic of gating for S-phase cells (n = 3,000 random cells displayed). A.U., arbitrary unit; R.F.U., relative fluorescence unit. **(H)** Rate of EdU incorporation was measured in S-phase cells as the median nuclear intensity and was normalized to control cells (sgCNTL). Error bars are population medians with 95% confidence intervals ($n \geq 8{,}659$ cells per condition). **(I)** LRR1 gene expression time course measured by RNA-Seq. Each time point contains three independent experiments (two experiments for 24-h time point). **(J)** Left: Serum-starved cells were released in the presence of DMSO or palbociclib, harvested, and blotted for LRR1 and known E2F targets TOP2A and GINS2. Arrowhead indicates LRR1-specific band; the other band is a nonspecific band. Right: Quantification of Western blots (relative to actin loading control), normalized to DMSO conditions. Paired Student's t test; P = 8.0×10^{-3}, 3.7×10^{-3} (n = 3 independent experiments). **(K)** E2F1 ChIP-Seq signal (blue plot, ENCODE ENCFF009LGS; data are representative of two independent experiments) and detected peaks (green line, ENCODE ENCFF998YJY, irreproducible discovery rate cutoff = 0.05). In all panels, **, P < 0.01; ***, P < 0.001.

LRR1 knockout results in failure to disassemble replisomes and reduced rate of DNA replication

To study the role of human LRR1 in helicase unloading, we performed immunofluorescence after detergent-based preextraction to quantify chromatin-bound proteins in thousands of single cells (Fig. 2 A; Forment and Jackson, 2015; Toledo et al., 2013). We verified that the protocol successfully extracted non–chromatin-bound proteins while leaving behind chromatin-bound proteins (Fig. S2 A). We found that knocking out LRR1 reduced the rate of DNA replication (Fig. 2 A and Fig. S2 B) and increased the abundance of chromatin-bound CDC45, a component of the vertebrate CMG helicase, during S phase (Fig. 2 B). As cells progressed through S phase, the suppression of DNA replication after LRR1 knockout became increasingly stronger (Fig. 2, C and D), and the abundance of chromatin-bound CDC45 increased (Fig. 2 E; R^2 = 0.65 in knockout cells vs. R^2 = 0.00 in control cells). We observed similar phenotypes (i) when we knocked out LRR1 in another nontransformed cell line, RPE-1 hTERT (retinal pigment epithelial cells; Fig. S2 C) and (ii) when we acutely inhibited p97 ATPase activity with the specific small-molecule inhibitor CB-5083 (Fig. S2 D; Anderson et al., 2015; Zhou et al., 2015).

By expressing CRISPR-resistant LRR1, we rescued both the DNA replication defect and elevated chromatin-bound CDC45 after LRR1 knockout (Fig. 2 F). Additionally, we stably knocked out endogenous LRR1 in cells expressing doxycycline-inducible CRISPR-resistant LRR1 and selected for single-cell clones (see Materials and methods/Stable LRR1 knockout cells). We combined an LRR1-targeting siRNA with doxycycline removal and achieved near-complete (~97%) depletion of LRR1 protein in *LRR1*$^{-/-}$ cells (Fig. 2 G, top, and Fig. S2 F), which resulted in a reduction in DNA replication rate and failure to unload CMG helicases from chromatin in S-phase cells (Fig. 2 G, middle and bottom).

To test whether additional replisome components are persistently bound to chromatin in the absence of LRR1, we knocked out LRR1 and stained for a subset of key replisome components after preextraction and fixation. We found that LRR1 knockout resulted in elevated chromatin binding of another CMG component GINS4, DNA polymerase ε, and a component of the fork protection complex Timeless (Fig. 2 H and Fig. S2 G). DNA polymerase ε is the major polymerase responsible for leading-strand DNA replication and directly binds the CMG helicase (Burgers and Kunkel, 2017; Johansson and Dixon, 2013). Timeless is a component of the fork protection complex, which binds to multiple replisome components including the MCM complex (Chou and Elledge, 2006; Gotter et al., 2007; Leman et al., 2010; Leman and Noguchi, 2012). We did not find increased chromatin binding of PCNA or DNA polymerase α or δ after LRR1 knockout (Fig. S2 G). We also did not observe changes in chromatin binding of an MCM complex subunit MCM2, but this was not unexpected due to the large excess of licensed origins that do not fire (Fragkos et al., 2015). These excess MCM complexes are not used for DNA replication under unperturbed conditions and are known to be removed by an LRR1-independent unloading mechanism (Jagannathan et al., 2014; Nishiyama et al., 2011).

These results suggest that LRR1 and p97 activity are required to unload CMG helicases from chromatin during S phase in human cells, similar to findings in worms and frogs (Dewar et al., 2017; Sonneville et al., 2017). In the absence of LRR1, cells fail to efficiently disassemble the replisome, and the post-termination replisome includes at least the CMG helicase, DNA polymerase ε, and the fork protection complex. Unexpectedly, our results show that LRR1 knockout or p97 inhibition causes an increasingly stronger suppression of DNA replication as cells progress through S phase.

Failure to disassemble replisomes after LRR1 loss suppresses DNA replication by blocking the recycling of replication factors

Next, we examined how a failure to unload CMG helicases in the absence of LRR1 suppresses DNA replication. We first tested whether DNA damage signaling is responsible for the suppression. We found a reduced rate of DNA replication after LRR1 knockout in p53-null cells (Fig. S3 A). In addition, p21 knockdown did not rescue the suppression of DNA replication (Fig. S3 B). Furthermore, inhibiting major known pathways of DNA replication stress response (ATM, DNA-PK, ATR–Chk1–Wee1) did not rescue the reduced rate of DNA replication (Fig. S3 C). Consistent with this result, when we depleted LRR1, S-phase cells did not accumulate single-stranded DNA (measured by chromatin-bound RPA1), phospho-RPA2-Ser33, phospho-Chk1-Ser317, or phospho-Chk2-Thr68 (Fig. S3 D). These results suggest that the suppression of DNA replication in the absence of LRR1 is not the result of p53–p21 pathway activation or canonical DNA replication stress signaling.

We next hypothesized that persistent chromatin binding of CMG helicases and other replisome components is blocking their

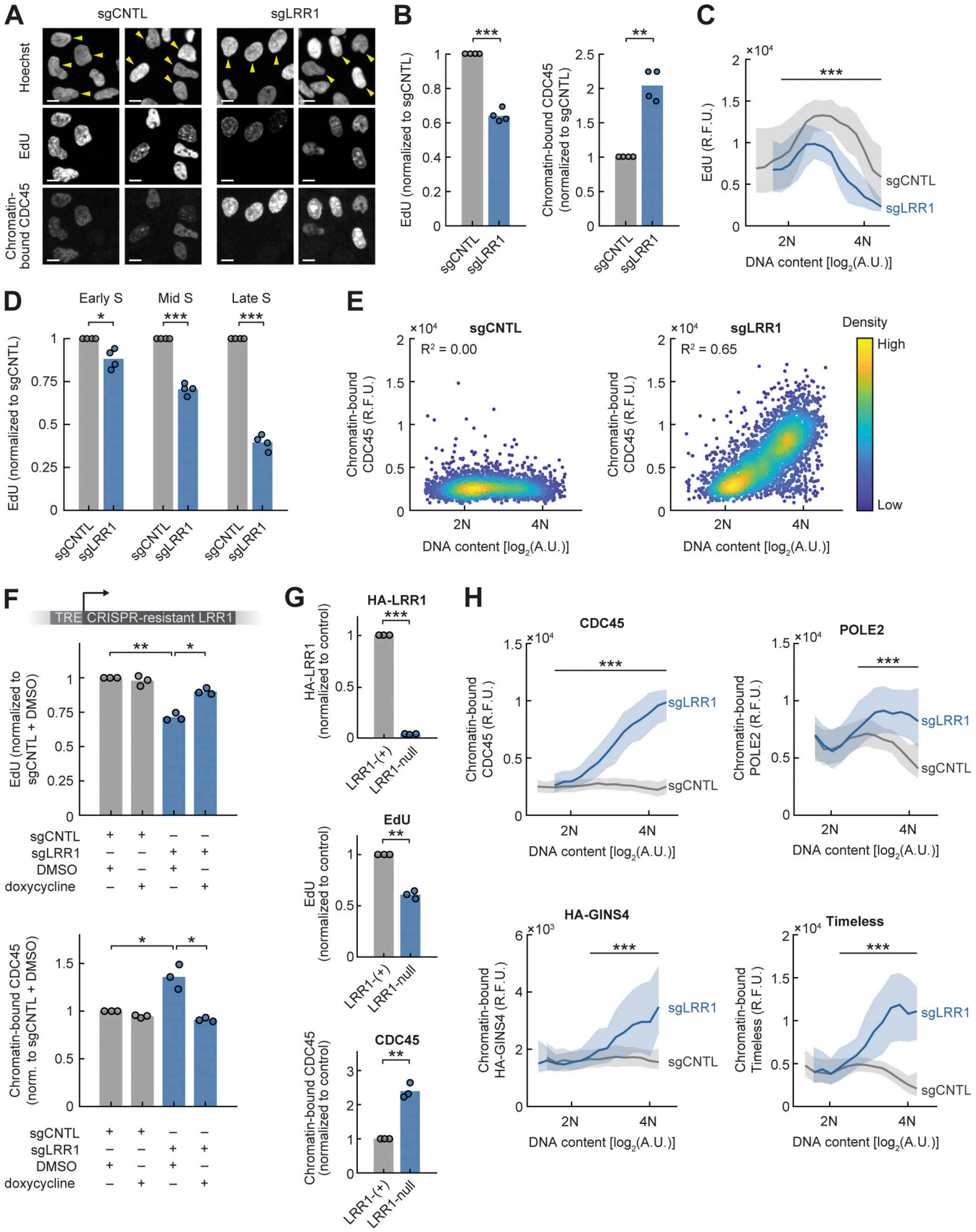

Figure 2. **LRR1 knockout results in failure to disassemble replisomes and reduced rate of DNA replication. (A)** Continuously cycling Cas9 cells were transfected with sgRNAs and fixed 1 d later, as in B–F and H. Sample immunofluorescence images are shown. Arrowheads indicate S-phase cells. Scale bar: 10 µm. Data are representative of four independent experiments. **(B)** Left: Rate of EdU incorporation in S-phase cells normalized to control cells (sgCNTL). Paired

Student's *t* test; P = 5.5 × 10^{-4} (*n* = 4 independent experiments, *n* ≥ 4,272 cells per condition). Right: Abundance of chromatin-bound CDC45 in S-phase cells normalized to control cells. Paired Student's *t* test; P = 1.1 × 10^{-3} (*n* = 4 independent experiments, *n* ≥ 4,272 cells per condition). **(C)** Rate of EdU incorporation in S-phase cells is plotted as a function of DNA content. Line plots are population medians in each bin; shaded error bars indicate 25th to 75th percentile (*n* ≥ 61 cells per bin, *n* = 9,393 and 6,182 cells total). Two-sample Student's *t* test; ***, P < 1 × 10^{-3}. Data are representative of four independent experiments. **(D)** Rate of EdU incorporation in early, mid, and late S-phase cells normalized to control cells. Early S: 2N–2.2N DNA, mid S: 2.9N–3.1N DNA, late S: 3.8N–4N DNA. Paired Student's *t* test; P = 0.030, 6.2 × 10^{-4}, 3.5 × 10^{-4} (*n* = 4 independent experiments, *n* ≥ 124 cells per condition). **(E)** Scatter plot of abundance of chromatin-bound CDC45 against DNA content in S-phase cells (R^2 = 0.00 and 0.65; P = 0.98, P < 1 × 10^{-3}; *n* = 3,000 random cells displayed). Data are representative of four independent experiments. **(F)** Top: Rate of EdU incorporation in S-phase cells normalized to control cells (sgCNTL + DMSO). Paired Student's *t* test; P = 4.4 × 10^{-3}, 0.015 (*n* = 3 independent experiments, *n* ≥ 4,993 cells per condition). Bottom: Abundance of chromatin-bound CDC45 in S-phase cells normalized to control cells. Paired Student's *t* test; P = 0.031, 0.028 (*n* = 3 independent experiments, *n* ≥ 4,993 cells per condition). TRE, tetracycline-responsive element. **(G)** LRR1 was depleted in *LRR1*$^{-/-}$ cells expressing exogenous, doxycycline-inducible LRR1 by removing doxycycline and transfecting siRNA targeting exogenous LRR1. As a negative control, the same cell line was treated with doxycycline and nontargeting siRNA. Nuclear fluorescence signals were normalized to control cells (LRR1 positive). Paired Student's *t* test; P = 5.9 × 10^{-4}, 5.3 × 10^{-3}, 3.5 × 10^{-3} (*n* = 3 independent experiments, *n* ≥ 1,041 cells per condition). **(H)** Abundance of chromatin-bound replisome components in S-phase cells is plotted as a function of DNA content. Line plots are population medians in each bin; shaded error bars indicate 25th to 75th percentile. Two-sample Student's *t* test; ***, P < 1 × 10^{-3}. CDC45: *n* ≥ 61 cells per bin, *n* ≥ 6,182 cells total. HA-GINS4: *n* ≥ 51 cells per bin, *n* ≥ 7,224 cells total. POLE2: *n* ≥ 71 cells per bin, *n* ≥ 4,647 cells total. Timeless: *n* ≥ 50 cells per bin, *n* ≥ 4,383 cells total. Data are representative of at least two independent experiments (HA-GINS4: two technical replicates). A.U., arbitrary unit; norm., normalized; R.F.U., relative fluorescence unit. In all panels, *, P < 0.05; **, P < 0.01; ***, P < 0.001.

recycling, thus depleting the soluble pool of rate-limiting factors required for efficient DNA replication. When we plotted the rate of DNA replication against the abundance of chromatin-bound CDC45, we found a positive correlation in control cells (Fig. 3 A, left; R^2 = 0.38), consistent with a rate-limiting role of CDC45 in origin firing (Fragkos et al., 2015; Köhler et al., 2016; Wong et al., 2011). But in cells transfected with sgRNA targeting LRR1, a population of cells showed increased binding of CDC45 to chromatin (indicative of successful LRR1 knockout), and the global rate of DNA replication was negatively correlated with the amount of chromatin-bound CDC45 in these cells (Fig. 3 A, shaded area on right; R^2 = −0.47). Furthermore, in each individual nucleus, EdU and chromatin-bound CDC45 stains were highly colocalized under control conditions, whereas the colocalization was weakened in cells with increased chromatin binding of CDC45 after LRR1 knockout (Fig. S4 A). These observations are consistent with the hypothesis that as more replisome components become stuck on chromatin after LRR1 knockout, the amounts of soluble components are reduced due to a lack of recycling, which then suppresses the initiation of DNA replication at other licensed origins.

To directly test this hypothesis, we performed subcellular fractionation to measure the abundance of replisome components in the soluble and insoluble pools (see Materials and methods/Subcellular fractionation). We synchronized cells at the G1/S boundary with the DNA polymerase inhibitor aphidicolin, and then we released cells from aphidicolin block for 5 h and harvested the cells (Fig. 3 B). Cell lysates were fractionated into detergent-soluble and insoluble pools, confirmed by GAPDH and histone H4 partitioning (Fig. 3 C). We blotted for replisome components (CDC45, GINS2, POLE1, Timeless, and MCM2) and quantified their abundance in soluble and insoluble fractions through LI-COR–based quantitative chemiluminescence detection. We found that LRR1 knockout resulted in increased levels of CDC45, GINS2, POLE1, and Timeless in the insoluble fraction while MCM2 was not affected (Fig. 3 C, compare lanes 2 and 4; and Fig. 3 D), consistent with results from preextraction-based immunofluorescence (Fig. 2 H and Fig. S2 G). Importantly, LRR1 knockout reduced the abundance of CDC45, POLE1, and Timeless in the soluble pool (Fig. 3 C, compare lanes 1 and 3; and Fig. 3 D). As a negative control, MCM2 level in the soluble fraction was not affected by LRR1 knockout (Fig. 3 D). Additionally, levels of replisome components in the soluble or insoluble fraction were not affected by LRR1 knockout when cells were not released from aphidicolin block (Fig. S4, B–D), suggesting that the depletion of replisome components from the soluble pool by LRR1 knockout is dependent on progression through S phase.

We note that the depletion of soluble replisome components after LRR1 knockout was not complete. Nevertheless, given the rate-limiting role of CDC45 in origin firing (Köhler et al., 2016; Wong et al., 2011) and haploinsufficiency of POLE1 during S-phase initiation (Pachlopnik Schmid et al., 2012), even an incomplete depletion of soluble factors is expected to reduce the rate of DNA replication. In addition, the bulk-cell measurement is an average of the cell population and likely underestimates the true extent of depletion due to incomplete knockout. We argue that these subcellular fractionation experiments provide direct evidence that LRR1 knockout causes a depletion of key replisome components from the soluble pool.

Next, we performed DNA fiber assays to investigate which steps of DNA replication were affected by the failure to disassemble replisomes after LRR1 loss (Fig. 3 E). Previous studies have reported a rate-limiting role for CDC45 (Köhler et al., 2016; Wong et al., 2011) and POLE1 (Bellelli et al., 2018) during origin firing in mammalian cells. As subcellular fractionation revealed reduced levels of soluble CDC45 and POLE1 after LRR1 loss, the defective recycling model predicts a lower rate of origin firing. We indeed found that fewer replication origins were activated after LRR1 depletion (Fig. 3 F, left), whereas fork progression was not affected (Fig. 3 F, right), suggesting that ongoing forks in LRR1-depleted cells are not stalled due to excessive DNA damage or collision with terminated replisomes that fail to disassemble. These results support the model that in the absence of LRR1-dependent replisome disassembly, the levels of soluble replisome components are reduced, which then suppresses the rate of origin firing.

Another prediction of the defective recycling model is that up-regulating the expression of rate-limiting replisome components

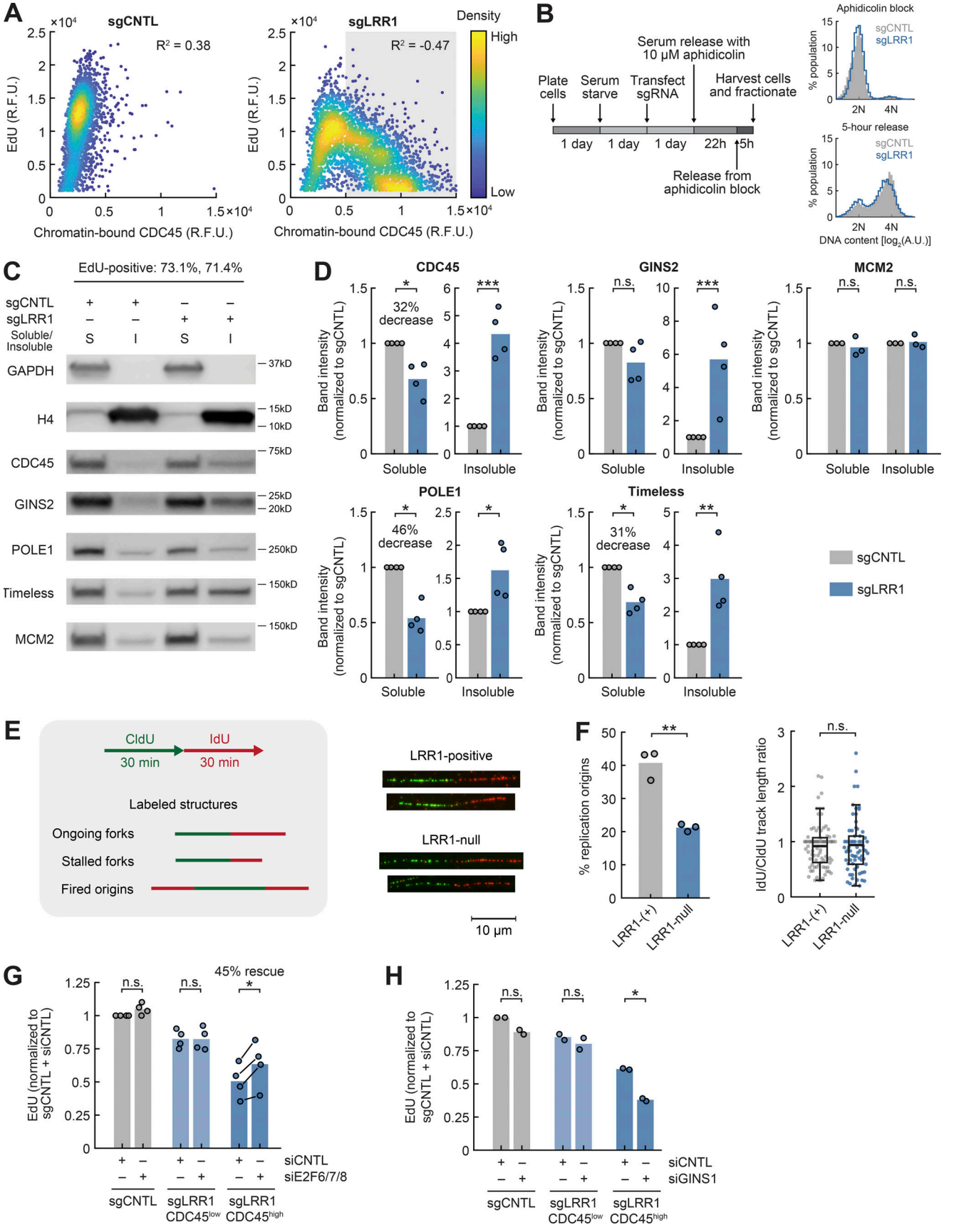

Figure 3. **Failure to disassemble replisomes after LRR1 loss suppresses DNA replication by blocking the recycling of replication factors. (A)** Continuously cycling Cas9 cells were transfected with sgRNAs and fixed 1 d later. Scatter plot of rate of EdU incorporation against abundance of chromatin-bound

CDC45 in S-phase cells (n = 3,000 random cells displayed). Left: R^2 = 0.38, P < 1 × 10^{-3}. Right: Shaded area represents cells with high chromatin-bound CDC45, where R^2 = −0.47, P < 1 × 10^{-3}. Data are representative of four independent experiments. **(B)** Left: Experimental setup. Right: Distribution of DNA content (n ≥ 17,152 cells per condition). **(C)** Cells were released for 5 h from an aphidicolin block and harvested. Detergent-soluble (S) and insoluble (I) proteins were fractionated and immunoblotted. Soluble and insoluble fractions were loaded at a ratio of 1:2. Data are representative of four independent experiments. **(D)** Quantification of Western blots (relative to GAPDH or H4 loading controls) normalized to control cells. Paired Student's t test; CDC45: P = 0.045, 7.1 × 10^{-4}; GINS2: P = 0.15, 0.014; POLE1: P = 0.011, 0.040; Timeless: P = 0.014, 7.0 × 10^{-3}; and MCM2: P = 0.53, 0.78 (n = 4 independent experiments). **(E)** Left: Schematic of DNA fiber assay. LRR1 was depleted in *LRR1*$^{-/-}$ cells expressing exogenous, doxycycline-inducible LRR1. Right: Sample images from DNA fiber assay. **(F)** Quantification of DNA fiber assay. Left: Percentage of total labeled structures that are replication origins. Two-sample Student's t test; P = 1.9 × 10^{-3} (n = 3 independent experiments, n ≥ 28 labeled structures per condition). Right: Ratio of IdU/CldU track lengths. Box plots represent the interquartile range (IQR), while whiskers represent the nonoutlier minimum and maximum; outliers are values that are more than 1.5 × IQR away from box edges. Two-sample Student's t test, P = 0.80; two-sample Kolmogorov-Smirnov test, P = 0.51 (data pooled from n = 3 independent experiments, n = 85 and 70 labeled tracks per condition). **(G)** Rate of EdU incorporation in S-phase cells normalized to control cells (sgCNTL + siCNTL). Cells were categorized as CDC45^{low} (unsuccessful knockout) or CDC45^{high} (successful knockout) based on the abundance of chromatin-bound CDC45. Paired Student's t test; P = 0.10, 0.77, 0.011 (n = 4 independent experiments, n ≥ 198 cells per condition). **(H)** Rate of EdU incorporation in S-phase cells normalized to control cells (sgCNTL + siCNTL). Paired Student's t test; P = 0.10, 0.27, 0.025 (n = 2 independent experiments, n ≥ 25 cells per condition). A.U., arbitrary unit; R.F.U., relative fluorescence unit. In all panels, *, P < 0.05; **, P < 0.01; ***, P < 0.001.

that are depleted from the soluble pool after LRR1 knockout would rescue the rate of DNA replication. We argued that as the vast majority of components in the post-termination replisome (including CDC45, GINS1~4, POLE1, POLE2, Timeless, TIPIN, and Claspin) are E2F transcriptional targets (Table S3 and Table S4), up-regulating E2F activity may increase the expression of multiple rate-limiting replisome components at the same time. To this end, we used siRNA to knock down combinations of E2F6, E2F7, and E2F8, which suppress the expression of E2F-responsive genes (Chen et al., 2009). We confirmed that knocking down E2F6/7/8 resulted in elevated expression of CDC45, Timeless, and POLE2 in S phase (Fig. S4 G). Next, we tested whether de-repressing E2F activity rescued DNA replication in LRR1 knockout cells. We found that knocking down E2F6/7/8 did not have an effect on the rate of DNA replication in cells transfected with control sgRNA (Fig. 3 G and Fig. S4 H, left bars). We stratified cells transfected with sgRNA targeting LRR1 into two populations: (i) a subset of cells that had elevated levels of chromatin-bound CDC45, indicating successful LRR1 knockout, and (ii) a subset with low levels of CDC45 that are comparable to control cells, reflecting unsuccessful knockout. Interestingly, E2F6/7/8 knockdown had no effect on the rate of DNA replication in cells with low levels of chromatin-bound CDC45 (Fig. 3 G and Fig. S4 H, middle bars). But in cells with high levels of chromatin-bound CDC45, E2F6/7/8 knockdown resulted in a partial rescue (45%) of the rate of DNA replication (Fig. 3 G and Fig. S4 H, right bars). This result supports the model where the failure to disassemble replisomes after LRR1 loss is depleting the soluble pool of rate-limiting factors required for efficient DNA replication. We note that de-repressing E2F activity only partially rescued the rate of DNA replication. This is likely due to (i) the failure to up-regulate potentially rate-limiting replisome components that are not E2F targets (e.g., POLE3, POLE4) and (ii) insufficient up-regulation of E2F-regulated rate-limiting factors compared with the level of soluble-pool depletion after LRR1 knockout.

Finally, we performed a synergy analysis by knocking down the CMG component GINS1 in combination with knocking out LRR1. We found that knocking down GINS1 alone did not reduce the rate of DNA replication in cells transfected with control sgRNA (Fig. 3 H, left bars). In cells transfected with sgRNA targeting LRR1, we again analyzed CDC45-high and CDC45-low populations. GINS1 knockdown had no effect on the rate of DNA replication in CDC45-low cells (Fig. 3 H, middle bars), whereas GINS1 knockdown led to a further reduction in the rate of DNA replication in CDC45-high cells (Fig. 3 H, right bars). The synergistic effect of LRR1 knockout and GINS component knockdown is again consistent with the defective recycling model. In LRR1 knockout cells, CDC45 and other replisome components (including GINS1) are sequestered on chromatin. This reduces the concentration of these components in the soluble pool, making them more sensitive to further down-regulation by siRNA knockdown.

We conclude from these experiments that loss of LRR1 causes a failure to unload CMG helicases and disassemble replisomes, which reduces the rate of DNA replication increasingly throughout S phase by sequestering rate-limiting replisome components on chromatin and blocking their recycling into the soluble pool.

Persistent binding of CMG helicases to chromatin after LRR1 loss blocks mitosis by activating ATR–Chk1–Wee1

Previous studies have reported that loss of *lrr-1* causes mitotic block in *C. elegans* germ cells (Burger et al., 2013; Merlet et al., 2010), whereas inhibition of CRL2^{LRR1} activity in frog egg extracts does not block mitotic entry (Priego Moreno et al., 2019). We tested whether LRR1-mediated CMG helicase unloading is required for mitosis in human cells. We transfected cells stably expressing Cas9 with nontargeting or LRR1-targeting sgRNA and measured chromatin-bound CDC45 and phospho-histone H3-Ser10, a canonical marker of mitosis (Fig. 4, A and B). We found that knocking out LRR1 led to accumulation of chromatin-bound CDC45 in G2/M cells and a significant reduction in the percentage of mitotic cells in the G2/M population (Fig. 4, C and D; and Fig. S5 A). Additionally, treatment with the p97 inhibitor CB-5083 also led to a mitotic block, phenocopying the LRR1 knockout (Fig. S5 B). We also measured the rate of mitosis by imaging live cells and identifying mitotic events by chromatin separation during anaphase (Fig. S5 C) and similarly found a mitotic block after knocking out LRR1 (Fig. S5, D and E). The mitotic block after LRR1 knockout was rescued by expressing CRISPR-resistant LRR1 (Fig. 4 E). These results suggest that loss

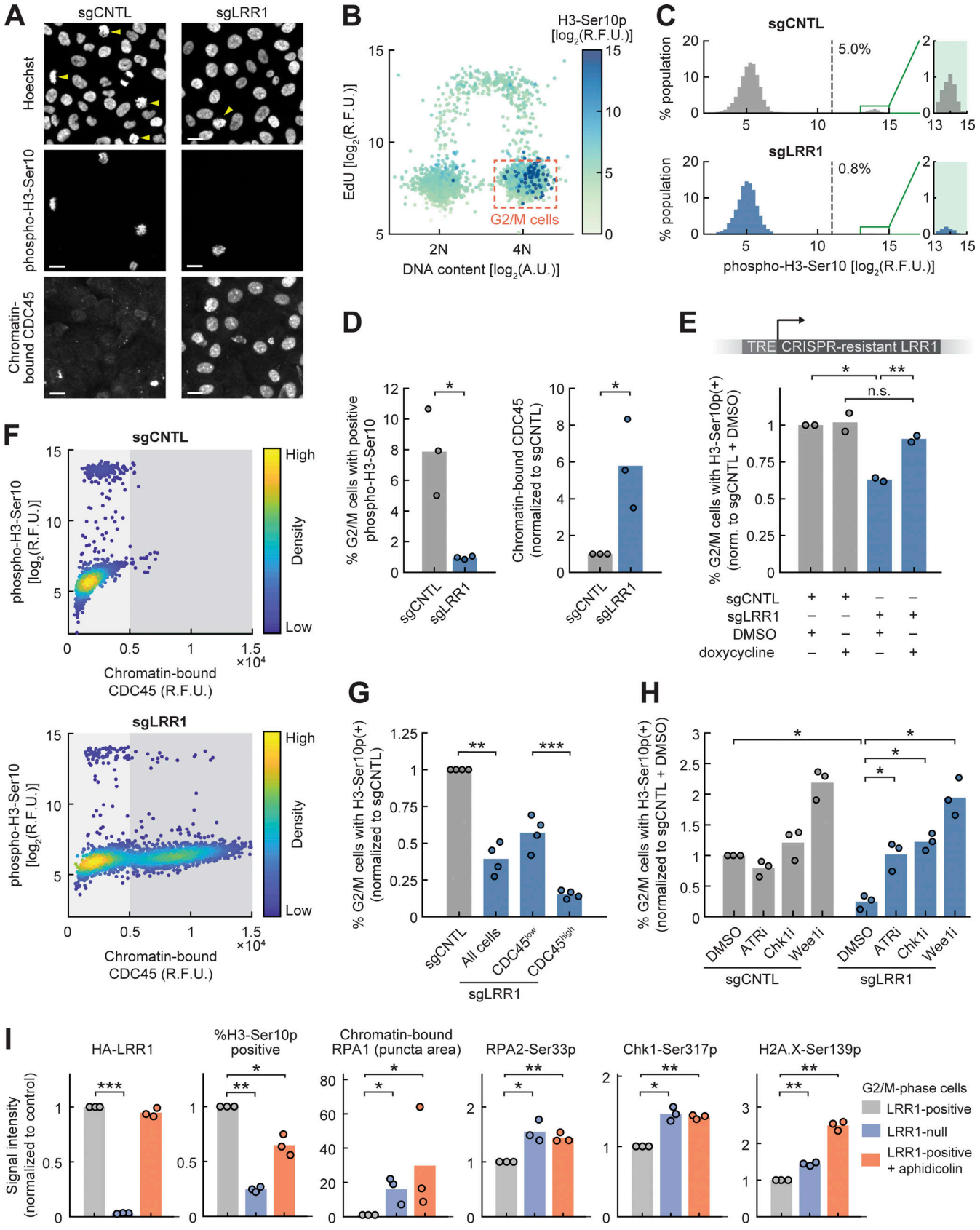

Figure 4. **Persistent binding of CMG helicases to chromatin after LRR1 loss blocks mitosis by activating ATR–Chk1–Wee1. (A)** Serum-starved Cas9 cells were transfected with sgRNAs, released from starvation, and fixed after 30 h. Sample immunofluorescence images are shown. Arrowheads indicate cells with positive phospho-H3-Ser10 signal. Scale bar: 20 µm. Data are representative of three independent experiments. **(B)** Schematic of gating for G2/M-phase

cells (n = 3,000 random cells displayed). **(C)** Histogram of phospho-H3-Ser10 signal in G2/M cells (cutoff = 11, $n \geq 4{,}389$ cells per condition). **(D)** Left: Percentage of G2/M cells with positive phospho-H3-Ser10 signal. Paired Student's t test; P = 0.048 (n = 3 independent experiments, $n \geq 4{,}389$ cells per condition). Right: Abundance of chromatin-bound CDC45 in G2/M-phase cells normalized to control cells. Paired Student's t test; P = 0.021 (n = 3 independent experiments, $n \geq 4{,}389$ cells per condition). **(E)** Continuously cycling Cas9 cells were transfected with sgRNAs and fixed 1 d later, as in F–H. Percentage of G2/M cells with positive phospho-H3-Ser10 signal normalized to control cells (sgCNTL + DMSO). Paired Student's t test, columns 1 vs. 3: P = 0.027; columns 3 vs. 4: $P = 6.9 \times 10^{-3}$; columns 2 vs. 4: P = 0.20 (n = 2 independent experiments, $n \geq 4{,}132$ cells per condition). **(F)** Scatter plot of phospho-H3-Ser10 signal against abundance of chromatin-bound CDC45 in G2/M-phase cells (n = 3,000 random cells displayed). Data are representative of three independent experiments. **(G)** Percentage of G2/M cells with positive phospho-H3-Ser10 signal was normalized to control cells. Cells were categorized as $CDC45^{low}$ or $CDC45^{high}$ based on the abundance of chromatin-bound CDC45 (see Fig. 4 F, light- and dark-shaded areas). Paired Student's t test; $P = 6.3 \times 10^{-3}$, 8.4×10^{-5} (n = 4 independent experiments, $n \geq 1{,}322$ cells per condition). **(H)** Cells were treated with the ATR inhibitor (ATRi; AZ20, 1 µM), Chk1 inhibitor (Chk1i; CHIR124, 500 nM), or Wee1 inhibitor (Wee1i; MK1775, 1 µM) for 4 h. Percentage of G2/M cells with positive phospho-H3-Ser10 signal was normalized to control cells (sgCNTL + DMSO). Paired Student's t test; P = 0.041, 0.012, 0.037, 0.011 (n = 3 independent experiments, $n \geq 2{,}804$ cells per condition). **(I)** LRR1 was depleted in *LRR1*$^{-/-}$ cells expressing exogenous, doxycycline-inducible LRR1. Positive control cells were treated with 10 µM aphidicolin for 3 h. The indicated protein markers were measured in G2/M cells through immunofluorescence, and nuclear signals were normalized to control cells (LRR1 positive). Paired Student's t test; *, P < 0.05; **, P < 0.01; *** P < 0.001 (n = 3 independent experiments, $n \geq 4{,}000$ cells per condition). A.U., arbitrary unit; norm., normalized; R.F.U., relative fluorescence unit; TRE, tetracycline-responsive element. In all panels, *, P < 0.05; **, P < 0.01; ***, P < 0.001.

of LRR1 in human cells leads to persistent chromatin-binding of CMG helicases in G2 phase and triggers a G2/M checkpoint that blocks mitosis.

Next, we tested whether and how the failure to unload CMG helicases from chromatin is linked to mitotic block. When we plotted the level of phospho-H3-Ser10 against chromatin-bound CDC45 in LRR1 knockout cells, we found that cells with higher levels of chromatin-bound CDC45 were less likely to progress into mitosis (Fig. 4, F and G). To identify the pathway responsible for mitotic block in LRR1 knockout cells, we first measured the mitotic rate after LRR1 knockout in either p53-null cells or cells where p21 was knocked down. We found that p53 knockout or p21 knockdown did not rescue the mitotic block after LRR1 knockout (Fig. S5, G and H), suggesting that the mitotic block was not p53/p21 dependent. Next, we treated cells with small-molecule inhibitors of major DNA damage signaling pathways and found that inhibiting the ATR–Chk1–Wee1 pathway rescued the mitotic block after LRR1 knockout (Fig. 4 H), whereas inhibiting ATM and DNA-PK did not (Fig. S5 I). Interestingly, while G2/M cells had high levels of chromatin-bound CDC45 after LRR1 knockout, cells that were forced through mitosis with Wee1 inhibition had basal levels of chromatin-bound CDC45 in G1 phase of the next cell cycle (Fig. S5 J). This suggests that human cells have an LRR1-independent backup pathway that engages during mitosis to unload remaining chromatin-bound CMG helicases if S-phase unloading fails, reminiscent of UBXN-3 and TRAIP-dependent pathways characterized in worms and frogs (Deng et al., 2019; Priego Moreno et al., 2019; Sonneville et al., 2019; Sonneville et al., 2017).

Finally, we assessed the types of DNA damage in G2/M cells caused by LRR1 knockout. Consistent with activation of the ATR–Chk1–Wee1 pathway, when we depleted LRR1, G2/M cells accumulated single-stranded DNA (measured by chromatin-bound RPA1), phospho-RPA2-Ser33, phospho-Chk1-Ser317, and γ-H2A.X (Fig. 4 I and Fig. S5 K). We also found that LRR1 depletion resulted in up-regulation of mitotic DNA synthesis, comparable to cells pretreated with aphidicolin (Fig. S5 L, top). Mitotic DNA synthesis has been reported to resolve under-replicated DNA at hard-to-replicate loci (Bergoglio et al., 2013; Minocherhomji et al., 2015), and failure to resolve under-replication during mitosis eventually leads to the formation of DNA lesions that are inherited by daughter cells and bound by 53BP1 nuclear bodies during G1 (Harrigan et al., 2011; Lukas et al., 2011; Spies et al., 2019). Upon completion of mitosis and arrival in G1 phase of the next cell cycle, LRR1-null cells did not accumulate chromatin-bound 53BP1 puncta, as opposed to cells pretreated with aphidicolin (Fig. S5 L, bottom). These results suggest that LRR1 depletion results in under-replicated DNA that accumulates in G2 phase, which is efficiently resolved through mitotic DNA synthesis and not inherited by daughter cells.

We conclude that in human cells, failure to unload CMG helicases after LRR1 loss activates the ATR–Chk1–Wee1 pathway and triggers a G2/M checkpoint, arresting cells in G2 and blocking mitosis.

LRR1 is an essential gene in normal and cancerous human cells

The DNA replication and mitotic defects in LRR1-deficient cells raise the question whether *LRR1* is an essential gene for the division of human cells. To assess the effect of LRR1 loss on long-term proliferation, we transfected nontransformed MCF10A cells stably expressing Cas9 with nontargeting or LRR1-targeting sgRNA and quantified cell proliferation by measuring cell number after 1 wk of culture. Indeed, LRR1 knockout resulted in a severe proliferation defect compared with control cells (Fig. 5 A).

To evaluate whether *LRR1* is more generally required for the division of human cells, we used a bioinformatics approach to analyze publicly available datasets from CRISPR gene essentiality screens in human cancer cells (Cancer DepMap, Broad Institute and Sanger Institute; Behan et al., 2019; Dempster et al., 2019 *Preprint*; Meyers et al., 2017). A gene knockout effect (CERES score) can be calculated for each gene in a specific cell line, and a larger negative score indicates that the gene is more likely an essential gene. In the CERES normalization scheme, the median score for nonessential genes is 0, while essential genes have a median score of −1. Strikingly, for all cell lines analyzed in the Broad and Sanger DepMap datasets, *LRR1* has gene knockout effects well below −1 (Fig. 5 B), a stronger effect than the majority of gold standard essential genes (Fig. 5 C). Similarly, a CRISPR gene essentiality screen performed in nontransformed retinal pigment epithelial cells (RPE-1 hTERT; Hart et al., 2015) also identified *LRR1* as a strong essential gene (Fig. 5 D). These

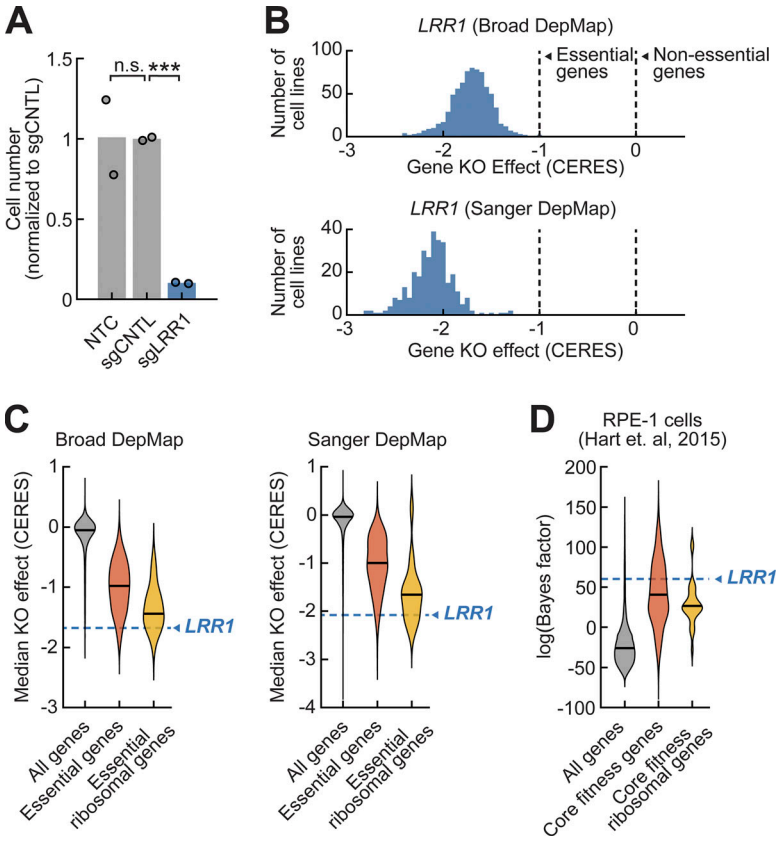

Figure 5. ***LRR1* is an essential gene in normal and cancerous human cells. (A)** Cell number after 7 d of culture normalized to control cells (sgCNTL). Two-sample Student's *t* test; n.s., P = 0.97; ***, P = 1.5 × 10^{-4} (*n* = 2 technical replicates). NTC, non-treated control, where cells were not transfected with sgRNAs. **(B)** Histogram of *LRR1* knockout (KO) effect (CERES score) in a panel of cancer cell lines from Broad and Sanger DepMap projects (*n* = 769 and 317 cell lines, DepMap Public 20Q2 release). A larger negative gene KO effect indicates that a gene is more likely to be essential in a given cell line. **(C)** Violin plot of median KO effect (across all cell lines) for all genes, essential genes, and essential ribosomal genes from Broad and Sanger DepMap projects. Dashed lines indicate median KO effect for *LRR1*. List of ribosomal genes is obtained from the HUGO Gene Nomenclature Committee. **(D)** Violin plot of Bayes factor for all genes, core fitness genes, and core fitness ribosomal genes in RPE-1 cells (Hart et al., 2015). Dashed line indicates Bayes factor for *LRR1*. A larger Bayes factor indicates that a gene is more likely to be essential.

results suggest that *LRR1* is an essential gene in normal and cancerous human cells that are actively dividing.

Discussion

Our study was motivated by a gene expression analysis of CDK4/6 activity-regulated genes followed by a targeted CRISPR screen, which unexpectedly showed that loss of the human *LRR1* gene strongly suppresses the rate of DNA replication. In our analysis of LRR1 function in human cells, we confirmed that LRR1 is required for unloading CMG helicases during S phase, which is consistent with its previously reported function in worms and frogs (Dewar et al., 2017; Sonneville et al., 2017). Additionally, a recent study published while this manuscript was under review showed that $CRL2^{LRR1}$ is the E3 ligase responsible for MCM7 polyubiquitination and CMG unloading during S phase in mouse embryonic stem cells (Villa et al., 2021). Our findings further argue for an evolutionarily conserved function of LRR1 in animals.

Interestingly, we found that loss of LRR1-dependent CMG helicase unloading suppresses the global rate of DNA replication in human cells. We show several lines of evidence that support a model where LRR1 loss results in persistent binding of replisome components to chromatin, thus blocking their recycling and depleting the soluble pool of rate-limiting factors required for efficient DNA replication (Fig. 6, top). After replisome disassembly, polyubiquitylated MCM7 is not degraded by the proteasome (Fullbright et al., 2016), and the GINS complex remains intact and can still interact with CDC45 (Deegan et al., 2020), suggesting that replisome components could be readily recycled for DNA replication at other licensed origins. The reduced rate of DNA replication after LRR1 loss in human cells is in contrast to previous studies using frog egg extracts where DNA synthesis was not affected by blocking CMG helicase unloading through immunodepletion of $CRL2^{LRR1}$ (Dewar et al., 2017; Sonneville et al., 2017), inhibition of polyubiquitylation (Dewar et al., 2015; Moreno et al., 2014; Sonneville et al., 2017), or inhibition of p97 ATPase activity (Moreno et al., 2014; Sonneville et al., 2017). It is likely that frog egg extracts contain large amounts of DNA replication factors relative to the amount of exogenous DNA added in replication assays, whereas the same factors are rate limiting in intact human cells.

In the absence of LRR1, CMG helicases are retained on chromatin in G2 phase, which results in activation of the ATR–Chk1–Wee1 pathway and the G2/M checkpoint (Fig. 6, bottom). Furthermore, we observed increased chromatin-binding of RPA1 in G2 (Fig. 4 I) and elevated DNA synthesis during mitosis (Fig. S5 L), suggesting that under-replicated DNA is present in G2/M (Bergoglio et al., 2013; Minocherhomji et al., 2015). We speculate that (i) chromatin-bound CMG helicases in G2 actively unwind double-stranded DNA into single-stranded DNA or (ii) single-stranded DNA accumulates in regions with under-replicated DNA (e.g., during double fork stalling events; Bertolin et al., 2020). Single-stranded DNA then recruits replication protein A (RPA) and triggers ATR activation (Saldivar et al., 2017). The exact mechanisms of single-stranded DNA accumulation and its implications on genome stability warrant further investigation.

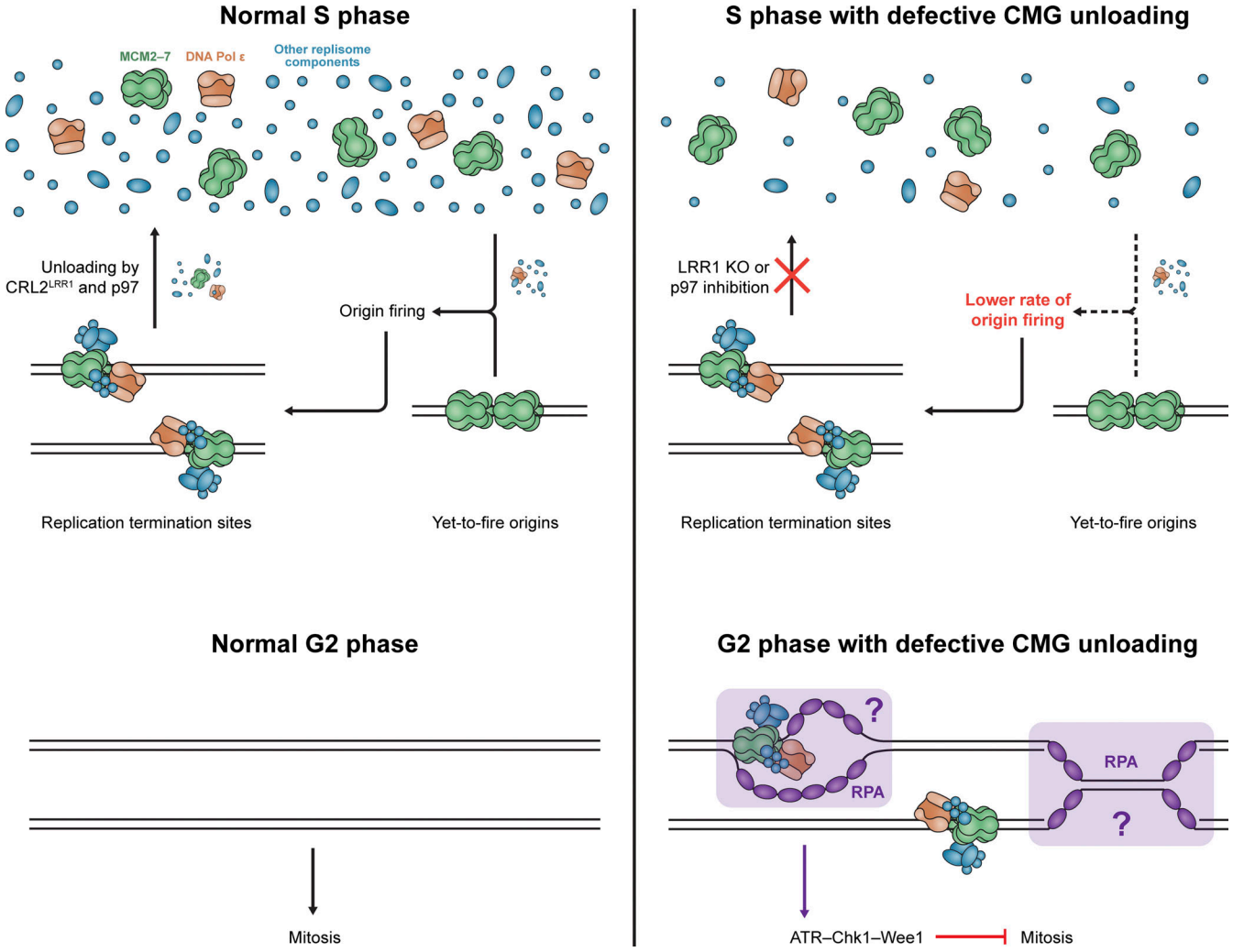

Figure 6. **Working model.** Recycling of replisome components back into the soluble pool after replication termination is blocked when CMG unloading and replisome disassembly are defective. This leads to lower rates of origin firing at yet-to-fire origins and reduced rate of DNA replication globally. Persistent binding of post-termination replisomes to chromatin during G2 results in accumulation of single-stranded DNA and activation of the ATR–Chk1–Wee1 pathway, which triggers the G2/M checkpoint and blocks entry into mitosis. The mechanism and exact DNA structures that generate single-stranded DNA and RPA binding require further study. KO, knockout; Pol, polymerase.

Here, we also considered alternative mechanisms other than our proposed model. Additional targets of $CRL2^{LRR1}$ other than MCM7 have been previously reported in human cells (Starostina et al., 2010; Wang et al., 2012). It is plausible that these or other unidentified targets of $CRL2^{LRR1}$ are responsible for the reduced rate of DNA replication and mitotic block in LRR1 knockout cells. We ruled out p21, a target of $CRL2^{LRR1}$ in worms and humans, as the mediator for S-phase and G2/M-phase phenotypes (Fig. S3 B and Fig. S5 H). In addition, we found that a small-molecule p97 inhibitor phenocopied LRR1 knockout in reducing the rate of DNA replication (Fig. S2 D) and blocking mitosis (Fig. S5 B). While p97 has a wide range of cellular targets (van den Boom and Meyer, 2018), the fact that we observed similar phenotypes after LRR1 knockout and p97 inhibition suggests that CMG unloading, a convergent process downstream of both $CRL2^{LRR1}$ and p97, is responsible for the DNA replication and mitosis phenotypes.

In our model, we propose that the reduced rate of DNA replication after LRR1 knockout is due to the failure to disassemble replisomes, which blocks the recycling of replisome components back into the soluble pool. It is plausible that persistent chromatin binding of replisome components after fork convergence hinders DNA replication through other mechanisms (e.g., fork stalling due to DNA damage or collision of ongoing forks with terminated replisomes that fail to disassemble). We ruled out checkpoint activation in S phase through inhibitor treatment and staining of damage markers (Fig. S3, C and D). DNA fiber assay also showed that fork progression was not affected after LRR1 knockout (Fig. 3 F). These negative results and the multiple lines of evidence supporting our model led us to favor our interpretation that LRR1-dependent replisome disassembly is critical for efficient DNA replication by recycling replisome components. Nevertheless, we acknowledge that alternative, secondary defects downstream of LRR1 loss may also contribute to the DNA replication defect. For example, CMG helicases that fail to unload from chromatin after replication termination or lagging strand fork collapse (Vrtis et al., 2021) may cause collisions with

transcriptional complexes, which may explain the mild increase in γ-H2A.X signal (Fig. S3 D).

Finally, we show through our own data and analysis of published CRISPR screens that *LRR1* is an essential gene in nontransformed and cancerous human cells that are actively dividing. This is consistent with suppressed DNA replication and defective mitotic entry we showed in LRR1 knockout cells. Cancer cells often suffer from high replication stress and DNA damage (Macheret and Halazonetis, 2015), and multiple studies have suggested that oncogene activation leads to increased firing of replication origins (Bester et al., 2011; Di Micco et al., 2006; Jones et al., 2013). An increased number of fired origins results in higher demand and exhaustion of nucleotide pools (Beck et al., 2012; Bester et al., 2011) and replication factors, including the single-stranded DNA-binding protein RPA (Toledo et al., 2013), leading to replication stress and DNA damage. Thus, we speculate that as a result of increased origin firing and higher demand for replication factors, cancer cells might be more sensitive to reduced levels of rate-limiting replisome components in the soluble pool upon loss of $CRL2^{LRR1}$ activity. Interestingly, knockdown of Timeless or other components of the fork protection complex in cancer cells impedes fork progression and cell proliferation in a checkpoint-independent manner (Bianco et al., 2019; Somyajit et al., 2017). We note that Timeless was sequestered on chromatin and reduced in the soluble pool after LRR1 knockout (Fig. 3 D), suggesting that inhibition of $CRL2^{LRR1}$ activity may potentially phenocopy the Timeless knockdown. It will be interesting to develop inhibitors of $CRL2^{LRR1}$ activity and test for cancer-specific efficacy of $CRL2^{LRR1}$ inhibition as a cancer therapeutic.

In summary, we find an evolutionarily conserved requirement for LRR1 in CMG helicase unloading and replisome disassembly during S phase in human cells. Unexpectedly, we show that failure to disassemble replisomes in the absence of LRR1 reduces the rate of DNA replication increasingly throughout S phase by sequestering rate-limiting replisome components on chromatin and blocking their recycling into the soluble pool. Additionally, failure to unload CMG helicases eventually blocks mitotic entry by triggering an ATR-mediated G2/M checkpoint response. We further provide evidence that *LRR1* is an essential gene in dividing human cells, suggesting that CMG helicase unloading is a critical cell-cycle process and inhibition of $CRL2^{LRR1}$ enzyme activity is a potential target for cancer therapy.

Materials and methods

Cell culture

All experiments were performed using MCF10A cells unless noted otherwise. MCF10A cells (obtained from American Type Culture Collection [ATCC]; CRL-10317) were cultured in phenol red-free DMEM/F12 (Invitrogen) supplemented with 5% horse serum (ATCC), 20 ng/ml EGF (PeproTech), 10 µg/ml insulin (Sigma-Aldrich), 0.5 µg/ml hydrocortisone (Sigma-Aldrich), 100 ng/ml cholera toxin (Sigma-Aldrich), 50 U/ml penicillin, and 50 µg/ml streptomycin (Thermo Fisher Scientific). MCF10A $p53^{-/-}$ cells were obtained from Horizon Discovery (HD 101–005). To serum starve cells, cells were cultured for 2–3 d in phenol red-free DMEM/F12 (Invitrogen) supplemented with 0.5 µg/ml hydrocortisone (Sigma-Aldrich), 100 ng/ml cholera toxin (Sigma-Aldrich), 0.3% bovine serum albumin (Sigma-Aldrich), 50 U/ml penicillin, and 50 µg/ml streptomycin (Thermo Fisher Scientific). To synchronize cells at the G1/S boundary, serum-starved cells were released with full growth media in the presence of 10 µM aphidicolin (Cayman Chemicals; 14007); to release cells from aphidicolin block, cells were washed three times with growth media. RPE-1 hTERT cells (obtained from ATCC; CRL-4000) were cultured in phenol red-free DMEM/F12 (Invitrogen) supplemented with 10% fetal bovine serum (Atlanta Biologicals), 10 µg/ml hygromycin B (InvivoGen), 50 U/ml penicillin, and 50 µg/ml streptomycin (Thermo Fisher Scientific).

Constructs

Cells were transduced with lentiviral vectors pLV-EF1a-histone 2B (H2B)-mTurquoise-IRES-PuroR and pCSII-hDHB (amino acids 994–1087)-mVenus (Spencer et al., 2013) as previously described; lentiCas9-Blast (Addgene plasmid #52962) was a gift from Feng Zhang (Massachusetts Institute of Technology, Cambridge, MA). To construct doxycycline-inducible expression constructs, human LRR1 (containing CRISPR-resistant PAM mutations), CDC45, and GINS4 cDNA were cloned into the lentiviral backbone pCW-TRE-PGK promoter-BlastR-T2A-rtTA, derived from pCW-Cas9-Blast (Addgene plasmid #83481), which was a gift from Mohan Babu (University of Regina, Regina, Canada).

Chemicals

Chemicals used were PD-0332991/palbociclib (Selleck Chemicals; S1116; used at 1 µM), CB-5083 (Selleck Chemicals; S8101; used at 4 µM), AZ-20 (Cayman Chemicals; 17589; used at 2 µM), CHIR124 (Cayman Chemicals; 16553; used at 500 nM), MK1775 (Cayman Chemicals; 21266; used at 1 µM), KU-60019 (Cayman Chemicals; 17502; used at 5 µM), NU7441 (Cayman Chemicals; 14881; used at 1 µM), (+)-Aphidicolin (Cayman Chemicals; 14007), and doxycycline hyclate (Sigma-Aldrich; D9891; used at 1 µg/ml).

RNA-Seq and analysis

RNA was extracted using RNeasy Mini Kit (QIAGEN) according to manufacturer's instructions. RNA quality control was performed using an Agilent Bioanalyzer 2100. Sequencing library preparation was performed at the Stanford Functional Genomics Facility using the KAPA Stranded mRNA-Seq Kit, with KAPA mRNA Capture Beads (Roche) according to manufacturer's instructions. Single-index 6-mer adapters were added, and the libraries were sequenced with 75-bp single-end reads on an Illumina NextSeq platform (Stanford Functional Genomics Facility).

Raw reads were mapped onto a human genome assembly (GRCh38) using TopHat2 (Kim et al., 2013) and assigned to individual genes using featureCounts (Liao et al., 2014). Differential expression analysis was performed using DESeq2 (Love et al., 2014). See Table S1, Table S2, and Table S3 for raw read counts, differential expression analysis results, and a list of CDK4/6-dependent genes. Raw read sequences and counts have

been deposited in the National Center for Biotechnology Information's Gene Expression Omnibus and are accessible through GEO Series accession no. GSE173509.

ChIP-Seq analysis of ENCODE datasets

ENCODE ChIP-Seq signal and peaks were downloaded from ENCODE (ENCODE Project Consortium, 2012; Davis et al., 2018) and, in experiments where ENCODE only provided raw signal but not processed peaks, from ReMap 2020 (Chèneby et al., 2020): E2F1 (ENCSR000EVJ, ENCSR563LLO), FOXM1 (ENCSR429QPP, ENCSR831EIW, ENCSR000BRU-ReMap, ENCSR000BTB-ReMap, ENCSR000BUJ-ReMap, ENCSR000BUS-ReMap), and MYBL2 (ENCSR162IEM, ENCSR000BRO-ReMap). Peaks were annotated and assigned to the nearest transcription start site (<2 kb) using HOMER (Heinz et al., 2010). Genes with ChIP peaks identified in both experiments (at least four for FOXM1) were called as a transcription factor target gene. See Table S4 for lists of target genes.

Enrichment analysis was performed using Fisher's exact test against all expressed genes in MCF10A cells (16,788 genes).

sgRNA and siRNA transfection

Annealing of tracrRNA (trans-activating CRISPR RNA) and crRNA (CRISPR RNA) was performed before sgRNA transfection: 95°C for 5 min, ramp down to 25°C (1°C/min). sgRNAs and siRNAs were forward transfected into cells using DharmaFect 1 (Dharmacon) according to manufacturer's instructions, at a final concentration of 20 nM (sgRNA) or 40 nM (siRNA). Cells were changed into growth media ∼6 h after transfection. tracrRNAs were obtained from IDT: Alt-R CRISPR-Cas9 tracrRNA, ATTO 550 (1075928; used in Fig. 1 and Fig. S1) and Dharmacon: Edit-R tracrRNA (U-002005-20; used in all other figures). crRNAs were obtained from Dharmacon: nontargeting control (U-007503-01-05, 5′-GTCGACGTTATTGCCGGTCG-3′), LRR1 (pooled from CM-016820-01: 5′-CTGCTGACAGAGGCTCAACA-3′, CM-016820-02: 5′-ATGAGCAGGAAGGCTCGGAC-3′, CM-016820-03: 5′-ATATCTGTCTAAGTAAGGTA-3′, CM-016820-04: 5′-GATGAAGCTACACTGTGAGG-3′), and other gene candidates in targeted CRISPR screen (see Table S5 for sequences, pools of four individual crRNAs were used). siRNAs were obtained from Dharmacon: nontargeting control siRNA pool (D-001810-10-05: 5′-GCCCUUCUCUGCAGUCAAG-3′, 5′-UGGUUUACAUGUUGUGUGA-3′, 5′-UGGUUUACAUGUUUUCUGA-3′, and 5′-UGGUUUACAUGUUUUCCUA-3′) and LRR1 (J-016820-11: 5′-ACACUGUGGUCUUAGUAGA-3′, targets both endogenous and CRISPR-resistant exogenous expression construct); pools of four individual siRNAs were used for p21, GINS1, E2F6, E2F7, and E2F8 (see Table S5 for sequences).

Stable LRR1 knockout cells

Cells expressing Cas9 and doxycycline-inducible, CRISPR-resistant LRR1 were transfected with nontargeting or LRR1-targeting sgRNAs. Single-cell clones were isolated through limiting dilution and cultured in the presence of doxycycline to maintain expression of exogenous LRR1. Genomic DNA was extracted using DNeasy Blood & Tissue Kit (QIAGEN) according to manufacturer's instructions, and exon 1 of *LRR1* was PCR amplified and Sanger sequenced (Sequetech). PCR and sequencing results both verified homozygous nonsense mutations in *LRR1*$^{-/-}$ clones. To stop the expression of exogenous LRR1, doxycycline was removed from the cells, which resulted in a reduction in the rate of DNA replication (Fig. S2 E) and mitotic rate (Fig. S5 F) in cells where endogenous LRR1 was stably knocked out. The reduction in DNA replication rate was mild after the removal of doxycycline, possibly due to incomplete transcriptional shutdown from the doxycycline-inducible promoter. To further deplete LRR1, *LRR1*$^{-/-}$ cells expressing exogenous LRR1 were transfected with LRR1-targeting siRNA along with doxycycline removal, which achieved near complete (∼97%) depletion of LRR1 protein (Fig. S2 F). As a negative control, *LRR1*$^{-/-}$ cells expressing exogenous LRR1 were treated with doxycycline and nontargeting siRNA. In experiments where LRR1 was depleted in *LRR1*$^{-/-}$ cells expressing exogenous LRR1, phenotypic assays were performed 1 d after LRR1 depletion (Fig. 2 G; Fig. 3, E and F; Fig. 4 I; Fig. S3 D; and Fig. S5, K and L).

Preextraction and immunofluorescence

To preextract soluble proteins, cells were treated with ice-cold preextraction buffer (0.2% Triton X-100, 1× Halt Protease Inhibitor Cocktail [Thermo Fisher Scientific; 78439] in PBS) on an ice block for 5 min (2 min for RPE-1 hTERT cells) and subsequently fixed as previously described (Forment and Jackson, 2015; Toledo et al., 2013). To preextract soluble RPA70, cells were treated with ice-cold preextraction buffer (0.2% Triton X-100, 1× Halt Protease Inhibitor Cocktail [Thermo Fisher Scientific; 78439] in cytoskeletal buffer: 10 mM Pipes, 100 mM NaCl, 300 mM sucrose, and 3 mM $MgCl_2$, pH 7.0) on an ice block for 2 min and subsequently fixed. Cells were fixed in 4% paraformaldehyde (PBS solution) for 15 min at room temperature and washed three times with PBS. For certain antibodies, cells were treated with ice-cold methanol for 15 min at 4°C and washed three times with PBS. When cells expressed fluorescent proteins that spectrally overlapped with fluorophores used in subsequent steps, cells were chemically bleached with 3% H_2O_2 and 20 mM HCl (in PBS; Lin et al., 2015) for 1 h at room temperature and washed three times with PBS.

Cells were permeabilized in 0.2% Triton X-100 (in PBS) for 15 min and blocked with blocking buffer (10% fetal bovine serum, 1% bovine serum albumin, 0.1% Triton X-100, and 0.01% NaN_3 in PBS) for 1 h at room temperature. Cells were stained overnight at 4°C with primary antibodies (diluted in blocking buffer), washed three times with PBS, and stained with fluorophore-conjugated secondary antibodies (diluted in blocking buffer) for 1 h. Cells were subsequently stained with Hoechst 33342 (Thermo Fisher Scientific; 1:10,000 in PBS) for 10 min and washed three times with PBS.

For EdU incorporation assays, cells were treated with growth media containing 10 mM EdU (Invitrogen; A10044) for 15 min at 37°C. To fluorescently label EdU, cells were treated with Click reaction solution (2 mM CuSO4, 25 mg/ml sodium ascorbate, 3 µM AF488-picolyl-azide [Click Chemistry Tools; 1276] or AF647-picolyl-azide [Click Chemistry Tools; 1300] in 1× TBS, pH 8.3) for 20–30 min at room temperature, as previously described (Jao and Salic, 2008).

Primary antibodies used for immunofluorescence in this study were rabbit anti-CDC45 (Cell Signaling Technology; 11881;

1:200; requires methanol treatment), mouse anti-PCNA (Santa Cruz Biotechnology; sc-56; 1:500; requires methanol treatment), rabbit anti-MCM2 (Cell Signaling Technology; 3619; 1:800), rabbit anti-POLA2 (Atlas Antibodies; HPA037570; 1:100), rabbit anti-POLD2 (Atlas Antibodies; HPA026745; 1:100), rabbit anti-POLE2 (Atlas Antibodies; HPA027555; 1:100), rabbit anti-Timeless (Abcam; ab109512; 1:800), mouse anti–phospho-histone H3-Ser10 (Cell Signaling Technology; 9706; 1:1,000), rabbit anti–phospho-histone H3-Ser10 (Cell Signaling Technology; 53348,; 1:1,000), rabbit anti-RPA70/RPA1 (Abcam; ab79398; 1:200), rabbit anti–phospho-RPA32/RPA2-Ser33 (Bethyl Laboratories; A300-246A; 1:1,000), rabbit anti–phospho-Chk1-Ser317 (Cell Signaling Technology; 12302; 1:800), rabbit anti–phospho-Chk2-Thr68 (Cell Signaling Technology; 2661; 1:100), rabbit anti–phospho-histone H2A.X-Ser139 (Cell Signaling Technology; 2577; 1:500), rabbit anti-53BP1 (Cell Signaling Technology; 4937; 1:500), rabbit anti-p21 (Cell Signaling Technology; 2947; 1:2,500), and rabbit anti-HA tag (Cell Signaling Technology; 3724; 1:1,000).

Secondary antibodies used for immunofluorescence in this study (1:1,000 dilution) were goat–anti-rabbit Alexa Fluor 555 (Thermo Fisher Scientific; A-21428), goat–anti-rabbit Alexa Fluor 647 (Thermo Fisher Scientific; A-21245), goat–anti-mouse Alexa Fluor 555 (Thermo Fisher Scientific; A-21424), and goat–anti-mouse Alexa Fluor 647 (Thermo Fisher Scientific; A-21235).

Imaging

Cells were plated onto glass-bottom 96-well plates (Cellvis; P96-1.5H-N), which were coated overnight with 60 µg/ml bovine collagen I (Advanced BioMatrix; #5005-B) for MCF10A cells or 20 µg/ml bovine plasma fibronectin (Sigma-Aldrich; F1141) for RPE-1 hTERT cells. Cells were imaged on an ImageXpress Micro microscope (Molecular Devices) in humidified 37°C chambers with 5% CO_2 and with the appropriate filter sets. 10× objective (0.3 N.A.) with no binning was used for live-cell imaging of H2B, cyclin E/A–CDK activity reporter; 20× objective (0.75 N.A.) with 2-by-2 pixel binning was used for fixed-cell immunofluorescence. MetaXpress software (Molecular Devices) and an Andor Zyla sCMOS camera were used for image acquisition. Cells were imaged in growth media during live-cell imaging and in PBS during fixed-cell imaging. During live-cell imaging, images were taken every 12 min or 15 min, with the total light exposure under 300 ms for each multicolor image.

Image analysis

Image analysis was performed with a custom MATLAB pipeline as previously described (Cappell et al., 2016; Chung et al., 2019). The code for the image analysis pipeline is available at https://github.com/scappell/Cell_tracking. Additional modified scripts are available from the corresponding author upon reasonable request. Briefly, optical illumination bias was corrected by measuring background autofluorescence signal for each imaging session, which was used to flatten the raw images. Global background subtraction was then performed on all images. Cell nuclei were segmented based on H2B-mTurquoise (live-cell imaging) or Hoechst (fixed-cell imaging). To measure the cyclin E/A–CDK activity reporter, the cytoplasm was sampled by expanding a ring outside the nucleus (with inner radius of 0.65 µm and outer radius of 3.25 µm) without overlapping with cytoplasm from a neighboring cell. The activity was calculated by taking the ratio between the median cytoplasmic intensity and the median nuclear intensity. For immunofluorescence quantification, DNA content was calculated as the total nuclear Hoechst intensity. Nuclear fluorescence signals were calculated as the median nuclear intensity. Nuclear puncta (RPA70, 53BP1, and EdU) were identified as the foreground by thresholding on background-subtracted images; puncta count was calculated as the number of foreground pixels. Spectral bleed-through was quantified and corrected by imaging cells stained with single fluorophores.

Subcellular fractionation and whole cell extraction

Detergent-soluble and insoluble protein fractions were separated using the Subcellular Protein Fractionation Kit for Cultured Cells (Thermo Fisher Scientific; 78840) with modifications (Fujita et al., 1997). Specifically, cells were trypsinized and washed with ice-cold PBS. After centrifugation (5 min at 500× *g*, 4°C), detergent-soluble proteins were extracted by lysing the cell pellet in ice-cold extraction buffer for 10 min at 4°C with shaking: cytoskeletal buffer (10 mM Pipes, 100 mM NaCl, 300 mM sucrose, and 3 mM $MgCl_2$, pH 7.0) supplemented with 0.5% Triton X-100 and Halt Protease and Phosphatase Inhibitor Cocktail (Thermo Fisher Scientific; 78442). After centrifugation (10 min at 15,000× *g*, 4°C), the supernatant was saved as the soluble fraction, and the pellet (insoluble fraction) was washed once in extraction buffer and resuspended in digestion buffer: nuclear extraction buffer (Thermo Fisher Scientific; 78840) supplemented with 5 mM $CaCl_2$, 3 U/µl micrococcal nuclease (Thermo Fisher Scientific; 78840) and Halt Protease and Phosphatase Inhibitor Cocktail (Thermo Fisher Scientific; 78442). The digestion reaction was incubated at 37°C for 15 min with frequent mixing. The soluble and insoluble fractions were mixed with 6× Laemmli sample buffer (0.375 M Tris, pH 6.8, 12% SDS, 60% glycerol, 0.6 M DTT, and 0.06% Bromophenol blue) and boiled at 95°C for 4 min.

GAPDH and histone H4 partitioning confirmed successful fractionation. In addition, immunofluorescence showed that CDC45, POLE2, Timeless, and MCM2 were all exclusively nuclear localized (Fig. S4 E), suggesting that the detergent-soluble fraction of these replisome components reflects the nucleoplasmic pool rather than the cytoplasmic pool.

Whole cell extracts were prepared by washing adherent cells with ice-cold PBS, followed by lysis in 1× Laemmli sample buffer and scraping. Chromatin was sheared using 25G insulin syringes, and samples were boiled at 95°C for 4 min.

Immunoblotting

Protein samples were separated by SDS-PAGE on 4–20% Tris-Glycine gels (Bio-Rad; 4561095) using Tris-Glycine SDS running buffer (Bio-Rad; 1610772). Proteins were then transferred onto polyvinylidene fluoride membranes (Bio-Rad; 1704156) by semi-dry transfer (Bio-Rad Trans-Blot Turbo). Membranes were washed with TBS with 0.1% Tween 20 (TBST) and blocked with TBST + 5% nonfat milk. Membranes were blotted with primary

antibodies diluted in TBST + 5% BSA + 0.01% NaN_3, washed with TBST, and blotted with HRP-conjugated secondary antibodies (Cell Signaling Technology; used at 1:5,000) diluted in TBST + 5% nonfat milk. Membranes were then incubated with chemiluminescent substrates according to manufacturer's instructions (SuperSignal West Pico; Thermo Fisher Scientific; 34080) and imaged using an Odyssey Fc Imaging System (LI-COR). Band intensity was quantified by subtracting off background from surrounding regions and summing up signal within the region of interest using Image Studio (LI-COR).

Antibodies used for immunoblotting in this study were rabbit anti-GAPDH (Cell Signaling Technology; 5174; 1:2,000), mouse anti-histone H4 (Abcam; ab31830; 1:1,000), rabbit anti-CDC45 (Cell Signaling Technology; 11881; 1:500), rabbit anti-GINS2 (Proteintech; 16247–1-AP; 1:1,000), mouse anti-DNA pol ε A (Santa Cruz Biotechnology; sc-390785; 1:200), rabbit anti-Timeless (Abcam; ab109512; 1:10,000), mouse anti-MCM2 (Cell Signaling Technology; 12079; 1:1,000), rabbit anti-LRR1 (Atlas Antibodies; HPA069364; 1:250), rabbit anti-TOP2A (Proteintech; 20233–1-AP; 1:500), and mouse anti-actin (Sigma-Aldrich; MAB1501; 1:4,000)

DNA fiber assay

DNA fiber assay was performed as previously described (Halliwell et al., 2020). Briefly, cells were sequentially pulse labeled with 25 µM CldU (Thermo Fisher Scientific; ICN10547883) followed by 250 µM IdU (Thermo Fisher Scientific; ICN10035701) for 30 min at 37°C. Cells were washed with ice-cold PBS, trypsinized, and resuspended at 2.5 × 10^6 cells/ml concentration in cold PBS. 2 µl of cell suspension was gently placed on a glass slide, and after incubation of 2–3 min, lysis buffer (200 mM Tris-HCl, pH 7.5, 50 mM EDTA, and 0.5% SDS) was added, followed by 2 min of incubation at room temperature. The slides were tilted at an angle (15°–45°) to allow the fibers to spread along the slide. After drying, the slides were fixed in methanol-acetic acid (3:1) for 15 min at −20°C, denatured in 2.5 M HCl for 30 min, and blocked in 5% BSA in 1X PBS for 20 min (blocking buffer). Primary anti-BrdU antibodies specific for CldU (Abcam; ab6326; 1:435) and IdU (BD Biosciences; 347580; 1:15) were applied for 1 h at room temperature followed by PBS wash. Slides were then stained with secondary antibodies, goat–anti-rat Alexa Fluor 488 (Invitrogen; A-11006; 1:15), and goat–anti-mouse Alexa Fluor 568 (Invitrogen; A-11031; 1:15) for 1 h at room temperature. Slides were mounted with ProLong Antifade Mountant (Thermo Fisher Scientific; P36930) and imaged on a Carl Zeiss Axio Imager M2 microscope. Labeled replication structures were identified and measured using ImageJ (National Institutes of Health).

Statistics

Statistical analyses were performed using Fisher's exact test (MATLAB fishertest), two-sample Kolmogorov-Smirnov test (MATLAB kstest2), Student's two-sample *t* test (MATLAB ttest2), or paired/one-sample *t* test (MATLAB ttest). Further details can be found in the figure legends. The following P value convention is used throughout the paper: n.s., $P > 0.05$; *, $P < 0.05$; **, $P < 0.01$; ***, $P < 0.001$.

Online supplemental material

Fig. S1 (related to Fig. 1) shows RNA-Seq analysis of CDK4/6 activity–regulated genes in MCF10A cells. Fig. S2 (related to Fig. 2) presents analysis of replisome disassembly and DNA replication after LRR1 loss. Fig. S3 (related to Fig. 3) shows suppression of DNA replication after LRR1 loss is not due to DNA damage signaling. Fig. S4 (related to Fig. 3) presents control experiments supporting the defective recycling model. Fig. S5 (related to Fig. 4) presents analysis of the G2/M checkpoint and under-replicated DNA after LRR1 loss. Table S1 shows raw RNA-Seq read counts for all genes and samples. Table S2 presents results from differential expression analysis of RNA-Seq experiments. Table S3 lists CDK4/6 activity-dependent genes and their manually annotated function. Table S4 lists target genes of E2F1, FOXM1, and MYBL2 identified from an analysis of publicly available ChIP-Seq results (ENCODE). Table S5 provides sequences of crRNAs and siRNAs used in this study.

Acknowledgments

We thank Mingyu Chung, Hee Won Yang, Katie Ferrick, Leighton Daigh, Lindsey Pack, Yumi Ida, and Tinghuan Chen for help with reagents and cell lines; members of the Meyer laboratory and Tomek Swigut for feedback and technical support; the Stanford Shared FACS Facility for cell sorting; and the Stanford Functional Genomics Facility for performing RNA-Seq.

This work was funded by a National Institute of General Medical Sciences R35 grant GM127026. Y. Fan was supported by the Stanford Graduate Fellowship and the Stanford Center for Systems Biology. M.S. Köberlin was supported by a postdoctoral fellowship from the Human Frontiers Science Program Organization. C. Liu and N. Ratnayeke were supported by a National Science Foundation Graduate Research Fellowship.

The authors declare no competing financial interests.

Author contributions: conceptualization, Y. Fan and T. Meyer; methodology, Y. Fan, M.S. Köberlin, N. Ratnayeke, C. Liu, M. Deshpande, J. Gerhardt, and T. Meyer; investigation, Y. Fan, M.S. Köberlin, N. Ratnayeke, C. Liu, and M. Deshpande; formal analysis, Y. Fan; writing, Y. Fan and T. Meyer; visualization, Y. Fan; supervision, J. Gerhardt and T. Meyer; funding acquisition, T. Meyer.

Submitted: 22 September 2020
Revised: 30 March 2021
Accepted: 4 May 2021

References

Anderson, D.J., R. Le Moigne, S. Djakovic, B. Kumar, J. Rice, S. Wong, J. Wang, B. Yao, E. Valle, S. Kiss von Soly, et al. 2015. Targeting the AAA ATPase p97 as an Approach to Treat Cancer through Disruption of Protein Homeostasis. *Cancer Cell.* 28:653–665. https://doi.org/10.1016/j.ccell.2015.10.002

Beck, H., V. Nähse-Kumpf, M.S. Larsen, K.A. O'Hanlon, S. Patzke, C. Holmberg, J. Mejlvang, A. Groth, O. Nielsen, R.G. Syljuåsen, and C.S. Sørensen. 2012. Cyclin-dependent kinase suppression by WEE1 kinase protects the genome through control of replication initiation and nucleotide consumption. *Mol. Cell. Biol.* 32:4226–4236. https://doi.org/10.1128/MCB.00412-12

Behan, F.M., F. Iorio, G. Picco, E. Gonçalves, C.M. Beaver, G. Migliardi, R. Santos, Y. Rao, F. Sassi, M. Pinnelli, et al. 2019. Prioritization of cancer therapeutic targets using CRISPR-Cas9 screens. *Nature.* 568:511–516. https://doi.org/10.1038/s41586-019-1103-9

Bell, S.P., and K. Labib. 2016. Chromosome Duplication in Saccharomyces cerevisiae. *Genetics.* 203:1027–1067. https://doi.org/10.1534/genetics.115.186452

Bellelli, R., V. Borel, C. Logan, J. Svendsen, D.E. Cox, E. Nye, K. Metcalfe, S.M. O'Connell, G. Stamp, H.R. Flynn, et al. 2018. Polε Instability Drives Replication Stress, Abnormal Development, and Tumorigenesis. *Mol. Cell.* 70:707–721.e7. https://doi.org/10.1016/j.molcel.2018.04.008

Bergoglio, V., A.S. Boyer, E. Walsh, V. Naim, G. Legube, M.Y. Lee, L. Rey, F. Rosselli, C. Cazaux, K.A. Eckert, and J.S. Hoffmann. 2013. DNA synthesis by Pol η promotes fragile site stability by preventing under-replicated DNA in mitosis. *J. Cell Biol.* 201:395–408. https://doi.org/10.1083/jcb.201207066

Bertolin, A.P., J.S. Hoffmann, and V. Gottifredi. 2020. Under-Replicated DNA: The Byproduct of Large Genomes? *Cancers (Basel).* 12:2764. https://doi.org/10.3390/cancers12102764

Bester, A.C., M. Roniger, Y.S. Oren, M.M. Im, D. Sarni, M. Chaoat, A. Bensimon, G. Zamir, D.S. Shewach, and B. Kerem. 2011. Nucleotide deficiency promotes genomic instability in early stages of cancer development. *Cell.* 145:435–446. https://doi.org/10.1016/j.cell.2011.03.044

Bianco, J.N., V. Bergoglio, Y.L. Lin, M.J. Pillaire, A.L. Schmitz, J. Gilhodes, A. Lusque, J. Mazières, M. Lacroix-Triki, T.I. Roumeliotis, et al. 2019. Overexpression of Claspin and Timeless protects cancer cells from replication stress in a checkpoint-independent manner. *Nat. Commun.* 10:910. https://doi.org/10.1038/s41467-019-08886-8

Bracken, A.P., M. Ciro, A. Cocito, and K. Helin. 2004. E2F target genes: unraveling the biology. *Trends Biochem. Sci.* 29:409–417. https://doi.org/10.1016/j.tibs.2004.06.006

Burger, J., J. Merlet, N. Tavernier, B. Richaudeau, A. Arnold, R. Ciosk, B. Bowerman, and L. Pintard. 2013. CRL2(LRR-1) E3-ligase regulates proliferation and progression through meiosis in the Caenorhabditis elegans germline. *PLoS Genet.* 9:e1003375. https://doi.org/10.1371/journal.pgen.1003375

Burgers, P.M.J., and T.A. Kunkel. 2017. Eukaryotic DNA Replication Fork. *Annu. Rev. Biochem.* 86:417–438. https://doi.org/10.1146/annurev-biochem-061516-044709

Cappell, S.D., M. Chung, A. Jaimovich, S.L. Spencer, and T. Meyer. 2016. Irreversible APC(Cdh1) Inactivation Underlies the Point of No Return for Cell-Cycle Entry. *Cell.* 166:167–180. https://doi.org/10.1016/j.cell.2016.05.077

Chen, H.Z., S.Y. Tsai, and G. Leone. 2009. Emerging roles of E2Fs in cancer: an exit from cell cycle control. *Nat. Rev. Cancer.* 9:785–797. https://doi.org/10.1038/nrc2696

Chèneby, J., Z. Ménétrier, M. Mestdagh, T. Rosnet, A. Douida, W. Rhalloussi, A. Bergon, F. Lopez, and B. Ballester. 2020. ReMap 2020: a database of regulatory regions from an integrative analysis of Human and Arabidopsis DNA-binding sequencing experiments. *Nucleic Acids Res.* 48(D1): D180–D188.

Chou, D.M., and S.J. Elledge. 2006. Tipin and Timeless form a mutually protective complex required for genotoxic stress resistance and checkpoint function. *Proc. Natl. Acad. Sci. USA.* 103:18143–18147. https://doi.org/10.1073/pnas.0609251103

Chung, M., C. Liu, H.W. Yang, M.S. Köberlin, S.D. Cappell, and T. Meyer. 2019. Transient Hysteresis in CDK4/6 Activity Underlies Passage of the Restriction Point in G1. *Mol. Cell.* 76:562–573.e4. https://doi.org/10.1016/j.molcel.2019.08.020

Costa, A., I.V. Hood, and J.M. Berger. 2013. Mechanisms for initiating cellular DNA replication. *Annu. Rev. Biochem.* 82:25–54. https://doi.org/10.1146/annurev-biochem-052610-094414

Davis, C.A., B.C. Hitz, C.A. Sloan, E.T. Chan, J.M. Davidson, I. Gabdank, J.A. Hilton, K. Jain, U.K. Baymuradov, A.K. Narayanan, et al. 2018. The Encyclopedia of DNA elements (ENCODE): data portal update. *Nucleic Acids Res.* 46(D1):D794–D801. https://doi.org/10.1093/nar/gkx1081

Deegan, T.D., P.P. Mukherjee, R. Fujisawa, C. Polo Rivera, and K. Labib. 2020. CMG helicase disassembly is controlled by replication fork DNA, replisome components and a ubiquitin threshold. *eLife.* 9:e60371. https://doi.org/10.7554/eLife.60371

Dempster, J.M., J. Rossen, M. Kazachkova, J. Pan, G. Kugener, D.E. Root, and A. Tsherniak. 2019. Extracting Biological Insights from the Project Achilles Genome-Scale CRISPR Screens in Cancer Cell Lines. *bioRxiv.* (Preprint posted July 31, 2019). https://doi.org/10.1101/720243

Deng, L., R.A. Wu, R. Sonneville, O.V. Kochenova, K. Labib, D. Pellman, and J.C. Walter. 2019. Mitotic CDK Promotes Replisome Disassembly, Fork Breakage, and Complex DNA Rearrangements. *Mol. Cell.* 73:915–929.e6. https://doi.org/10.1016/j.molcel.2018.12.021

Dewar, J.M., and J.C. Walter. 2017. Mechanisms of DNA replication termination. *Nat. Rev. Mol. Cell Biol.* 18:507–516. https://doi.org/10.1038/nrm.2017.42

Dewar, J.M., M. Budzowska, and J.C. Walter. 2015. The mechanism of DNA replication termination in vertebrates. *Nature.* 525:345–350. https://doi.org/10.1038/nature14887

Dewar, J.M., E. Low, M. Mann, M. Räschle, and J.C. Walter. 2017. CRL2^{Lrr1} promotes unloading of the vertebrate replisome from chromatin during replication termination. *Genes Dev.* 31:275–290. https://doi.org/10.1101/gad.291799.116

Di Micco, R., M. Fumagalli, A. Cicalese, S. Piccinin, P. Gasparini, C. Luise, C. Schurra, M. Garre', P.G. Nuciforo, A. Bensimon, et al. 2006. Oncogene-induced senescence is a DNA damage response triggered by DNA hyper-replication. *Nature.* 444:638–642. https://doi.org/10.1038/nature05327

Dimova, D.K., and N.J. Dyson. 2005. The E2F transcriptional network: old acquaintances with new faces. *Oncogene.* 24:2810–2826. https://doi.org/10.1038/sj.onc.1208612

ENCODE Project Consortium. 2012. An integrated encyclopedia of DNA elements in the human genome. *Nature.* 489:57–74. https://doi.org/10.1038/nature11247

Fischer, M., and G.A. Müller. 2017. Cell cycle transcription control: DREAM/MuvB and RB-E2F complexes. *Crit. Rev. Biochem. Mol. Biol.* 52:638–662. https://doi.org/10.1080/10409238.2017.1360836

Forment, J.V., and S.P. Jackson. 2015. A flow cytometry-based method to simplify the analysis and quantification of protein association to chromatin in mammalian cells. *Nat. Protoc.* 10:1297–1307. https://doi.org/10.1038/nprot.2015.066

Fragkos, M., O. Ganier, P. Coulombe, and M. Méchali. 2015. DNA replication origin activation in space and time. *Nat. Rev. Mol. Cell Biol.* 16:360–374. https://doi.org/10.1038/nrm4002

Franz, A., M. Orth, P.A. Pirson, R. Sonneville, J.J. Blow, A. Gartner, O. Stemmann, and T. Hoppe. 2011. CDC-48/p97 coordinates CDT-1 degradation with GINS chromatin dissociation to ensure faithful DNA replication. *Mol. Cell.* 44:85–96. https://doi.org/10.1016/j.molcel.2011.08.028

Fujita, M., T. Kiyono, Y. Hayashi, and M. Ishibashi. 1997. In vivo interaction of human MCM heterohexameric complexes with chromatin. Possible involvement of ATP. *J. Biol. Chem.* 272:10928–10935. https://doi.org/10.1074/jbc.272.16.10928

Fullbright, G., H.B. Rycenga, J.D. Gruber, and D.T. Long. 2016. p97 Promotes a Conserved Mechanism of Helicase Unloading during DNA Cross-Link Repair. *Mol. Cell. Biol.* 36:2983–2994. https://doi.org/10.1128/MCB.00434-16

Gotter, A.L., C. Suppa, and B.S. Emanuel. 2007. Mammalian TIMELESS and Tipin are evolutionarily conserved replication fork-associated factors. *J. Mol. Biol.* 366:36–52. https://doi.org/10.1016/j.jmb.2006.10.097

Halliwell, J.A., P. Gravells, and H.E. Bryant. 2020. DNA Fiber Assay for the Analysis of DNA Replication Progression in Human Pluripotent Stem Cells. *Curr. Protoc. Stem Cell Biol.* 54:e115. https://doi.org/10.1002/cpsc.115

Harrigan, J.A., R. Belotserkovskaya, J. Coates, D.S. Dimitrova, S.E. Polo, C.R. Bradshaw, P. Fraser, and S.P. Jackson. 2011. Replication stress induces 53BP1-containing OPT domains in G1 cells. *J. Cell Biol.* 193:97–108. https://doi.org/10.1083/jcb.201011083

Hart, T., M. Chandrashekhar, M. Aregger, Z. Steinhart, K.R. Brown, G. MacLeod, M. Mis, M. Zimmermann, A. Fradet-Turcotte, S. Sun, et al. 2015. High-Resolution CRISPR Screens Reveal Fitness Genes and Genotype-Specific Cancer Liabilities. *Cell.* 163:1515–1526. https://doi.org/10.1016/j.cell.2015.11.015

Heinz, S., C. Benner, N. Spann, E. Bertolino, Y.C. Lin, P. Laslo, J.X. Cheng, C. Murre, H. Singh, and C.K. Glass. 2010. Simple combinations of lineage-determining transcription factors prime cis-regulatory elements required for macrophage and B cell identities. *Mol. Cell.* 38:576–589. https://doi.org/10.1016/j.molcel.2010.05.004

Jagannathan, M., T. Nguyen, D. Gallo, N. Luthra, G.W. Brown, V. Saridakis, and L. Frappier. 2014. A role for USP7 in DNA replication. *Mol. Cell. Biol.* 34:132–145. https://doi.org/10.1128/MCB.00639-13

Jao, C.Y., and A. Salic. 2008. Exploring RNA transcription and turnover in vivo by using click chemistry. *Proc. Natl. Acad. Sci. USA.* 105:15779–15784. https://doi.org/10.1073/pnas.0808480105

Johansson, E., and N. Dixon. 2013. Replicative DNA polymerases. *Cold Spring Harb. Perspect. Biol.* 5:a012799. https://doi.org/10.1101/cshperspect.a012799

Jones, R.M., O. Mortusewicz, I. Afzal, M. Lorvellec, P. García, T. Helleday, and E. Petermann. 2013. Increased replication initiation and conflicts with transcription underlie Cyclin E-induced replication stress. *Oncogene*. 32: 3744–3753. https://doi.org/10.1038/onc.2012.387

Kim, D., G. Pertea, C. Trapnell, H. Pimentel, R. Kelley, and S.L. Salzberg. 2013. TopHat2: accurate alignment of transcriptomes in the presence of insertions, deletions and gene fusions. *Genome Biol.* 14:R36. https://doi.org/10.1186/gb-2013-14-4-r36

Köhler, C., D. Koalick, A. Fabricius, A.C. Parplys, K. Borgmann, H. Pospiech, and F. Grosse. 2016. Cdc45 is limiting for replication initiation in humans. *Cell Cycle*. 15:974–985. https://doi.org/10.1080/15384101.2016.1152424

Laoukili, J., M.R. Kooistra, A. Brás, J. Kauw, R.M. Kerkhoven, A. Morrison, H. Clevers, and R.H. Medema. 2005. FoxM1 is required for execution of the mitotic programme and chromosome stability. *Nat. Cell Biol.* 7:126–136. https://doi.org/10.1038/ncb1217

Leman, A.R., and E. Noguchi. 2012. Local and global functions of Timeless and Tipin in replication fork protection. *Cell Cycle*. 11:3945–3955. https://doi.org/10.4161/cc.21989

Leman, A.R., C. Noguchi, C.Y. Lee, and E. Noguchi. 2010. Human Timeless and Tipin stabilize replication forks and facilitate sister-chromatid cohesion. *J. Cell Sci.* 123:660–670. https://doi.org/10.1242/jcs.057984

Liao, Y., G.K. Smyth, and W. Shi. 2014. featureCounts: an efficient general purpose program for assigning sequence reads to genomic features. *Bioinformatics*. 30:923–930. https://doi.org/10.1093/bioinformatics/btt656

Limas, J.C., and J.G. Cook. 2019. Preparation for DNA replication: the key to a successful S phase. *FEBS Lett.* 593:2853–2867. https://doi.org/10.1002/1873-3468.13619

Lin, J.R., M. Fallahi-Sichani, and P.K. Sorger. 2015. Highly multiplexed imaging of single cells using a high-throughput cyclic immunofluorescence method. *Nat. Commun.* 6:8390. https://doi.org/10.1038/ncomms9390

Liu, C., Y. Konagaya, M. Chung, L.H. Daigh, Y. Fan, H.W. Yang, K. Terai, M. Matsuda, and T. Meyer. 2020. Altered G1 signaling order and commitment point in cells proliferating without CDK4/6 activity. *Nat. Commun.* 11:5305. https://doi.org/10.1038/s41467-020-18966-9

Love, M.I., W. Huber, and S. Anders. 2014. Moderated estimation of fold change and dispersion for RNA-seq data with DESeq2. *Genome Biol.* 15: 550. https://doi.org/10.1186/s13059-014-0550-8

Low, E., G. Chistol, M.S. Zaher, O.V. Kochenova, and J.C. Walter. 2020. The DNA replication fork suppresses CMG unloading from chromatin before termination. *Genes Dev.* 34:1534–1545. https://doi.org/10.1101/gad.339739.120

Lukas, C., V. Savic, S. Bekker-Jensen, C. Doil, B. Neumann, R.S. Pedersen, M. Grøfte, K.L. Chan, I.D. Hickson, J. Bartek, and J. Lukas. 2011. 53BP1 nuclear bodies form around DNA lesions generated by mitotic transmission of chromosomes under replication stress. *Nat. Cell Biol.* 13: 243–253. https://doi.org/10.1038/ncb2201

Macheret, M., and T.D. Halazonetis. 2015. DNA replication stress as a hallmark of cancer. *Annu. Rev. Pathol.* 10:425–448. https://doi.org/10.1146/annurev-pathol-012414-040424

Malumbres, M., and M. Barbacid. 2001. To cycle or not to cycle: a critical decision in cancer. *Nat. Rev. Cancer*. 1:222–231. https://doi.org/10.1038/35106065

Maric, M., T. Maculins, G. De Piccoli, and K. Labib. 2014. Cdc48 and a ubiquitin ligase drive disassembly of the CMG helicase at the end of DNA replication. *Science*. 346:1253596. https://doi.org/10.1126/science.1253596

Merlet, J., J. Burger, N. Tavernier, B. Richaudeau, J.E. Gomes, and L. Pintard. 2010. The CRL2LRR-1 ubiquitin ligase regulates cell cycle progression during C. elegans development. *Development*. 137:3857–3866. https://doi.org/10.1242/dev.054866

Meyers, R.M., J.G. Bryan, J.M. McFarland, B.A. Weir, A.E. Sizemore, H. Xu, N.V. Dharia, P.G. Montgomery, G.S. Cowley, S. Pantel, et al. 2017. Computational correction of copy number effect improves specificity of CRISPR-Cas9 essentiality screens in cancer cells. *Nat. Genet.* 49: 1779–1784. https://doi.org/10.1038/ng.3984

Minocherhomji, S., S. Ying, V.A. Bjerregaard, S. Bursomanno, A. Aleliunaite, W. Wu, H.W. Mankouri, H. Shen, Y. Liu, and I.D. Hickson. 2015. Replication stress activates DNA repair synthesis in mitosis. *Nature*. 528: 286–290. https://doi.org/10.1038/nature16139

Moreno, S.P., R. Bailey, N. Campion, S. Herron, and A. Gambus. 2014. Polyubiquitylation drives replisome disassembly at the termination of DNA replication. *Science*. 346:477–481. https://doi.org/10.1126/science.1253585

Nishiyama, A., L. Frappier, and M. Méchali. 2011. MCM-BP regulates unloading of the MCM2-7 helicase in late S phase. *Genes Dev.* 25:165–175. https://doi.org/10.1101/gad.614411

Pachlopnik Schmid, J., R. Lemoine, N. Nehme, V. Cormier-Daire, P. Revy, F. Debeurme, M. Debré, P. Nitschke, C. Bole-Feysot, L. Legeai-Mallet, et al. 2012. Polymerase ε1 mutation in a human syndrome with facial dysmorphism, immunodeficiency, livedo, and short stature ("FILS syndrome"). *J. Exp. Med.* 209:2323–2330. https://doi.org/10.1084/jem.20121303

Priego Moreno, S., R.M. Jones, D. Poovathumkadavil, S. Scaramuzza, and A. Gambus. 2019. Mitotic replisome disassembly depends on TRAIP ubiquitin ligase activity. *Life Sci. Alliance*. 2:e201900390. https://doi.org/10.26508/lsa.201900390

Sadasivam, S., S. Duan, and J.A. DeCaprio. 2012. The MuvB complex sequentially recruits B-Myb and FoxM1 to promote mitotic gene expression. *Genes Dev.* 26:474–489. https://doi.org/10.1101/gad.181933.111

Saldivar, J.C., D. Cortez, and K.A. Cimprich. 2017. The essential kinase ATR: ensuring faithful duplication of a challenging genome. *Nat. Rev. Mol. Cell Biol.* 18:622–636. https://doi.org/10.1038/nrm.2017.67

Somyajit, K., R. Gupta, H. Sedlackova, K.J. Neelsen, F. Ochs, M.B. Rask, C. Choudhary, and J. Lukas. 2017. Redox-sensitive alteration of replisome architecture safeguards genome integrity. *Science*. 358:797–802. https://doi.org/10.1126/science.aao3172

Sonneville, R., S.P. Moreno, A. Knebel, C. Johnson, C.J. Hastie, A. Gartner, A. Gambus, and K. Labib. 2017. CUL-2^{LRR-1} and UBXN-3 drive replisome disassembly during DNA replication termination and mitosis. *Nat. Cell Biol.* 19:468–479. https://doi.org/10.1038/ncb3500

Sonneville, R., R. Bhowmick, S. Hoffmann, N. Mailand, I.D. Hickson, and K. Labib. 2019. TRAIP drives replisome disassembly and mitotic DNA repair synthesis at sites of incomplete DNA replication. *eLife*. 8:48686. https://doi.org/10.7554/eLife.48686

Spencer, S.L., S.D. Cappell, F.C. Tsai, K.W. Overton, C.L. Wang, and T. Meyer. 2013. The proliferation-quiescence decision is controlled by a bifurcation in CDK2 activity at mitotic exit. *Cell*. 155:369–383. https://doi.org/10.1016/j.cell.2013.08.062

Spies, J., C. Lukas, K. Somyajit, M.B. Rask, J. Lukas, and K.J. Neelsen. 2019. 53BP1 nuclear bodies enforce replication timing at under-replicated DNA to limit heritable DNA damage. *Nat. Cell Biol.* 21:487–497. https://doi.org/10.1038/s41556-019-0293-6

Starostina, N.G., J.M. Simpliciano, M.A. McGuirk, and E.T. Kipreos. 2010. CRL2(LRR-1) targets a CDK inhibitor for cell cycle control in C. elegans and actin-based motility regulation in human cells. *Dev. Cell*. 19:753–764. https://doi.org/10.1016/j.devcel.2010.10.013

Toledo, L.I., M. Altmeyer, M.B. Rask, C. Lukas, D.H. Larsen, L.K. Povlsen, S. Bekker-Jensen, N. Mailand, J. Bartek, and J. Lukas. 2013. ATR prohibits replication catastrophe by preventing global exhaustion of RPA. *Cell*. 155:1088–1103. https://doi.org/10.1016/j.cell.2013.10.043

van den Boom, J., and H. Meyer. 2018. VCP/p97-Mediated Unfolding as a Principle in Protein Homeostasis and Signaling. *Mol. Cell*. 69:182–194. https://doi.org/10.1016/j.molcel.2017.10.028

Villa, F., R. Fujisawa, J. Ainsworth, K. Nishimura, M. Lie-A-Ling, G. Lacaud, and K.P. Labib. 2021. CUL2^{LRR1}, TRAIP and p97 control CMG helicase disassembly in the mammalian cell cycle. *EMBO Rep.* 22:e52164. https://doi.org/10.15252/embr.202052164

Vrtis, K.B., J.M. Dewar, G. Chistol, R.A. Wu, T.G.W. Graham, and J.C. Walter. 2021. Single-strand DNA breaks cause replisome disassembly. *Mol. Cell*. 81:1309–1318.e6. https://doi.org/10.1016/j.molcel.2020.12.039

Wang, I.C., Y.J. Chen, D. Hughes, V. Petrovic, M.L. Major, H.J. Park, Y. Tan, T. Ackerson, and R.H. Costa. 2005. Forkhead box M1 regulates the transcriptional network of genes essential for mitotic progression and genes encoding the SCF (Skp2-Cks1) ubiquitin ligase. *Mol. Cell. Biol.* 25: 10875–10894. https://doi.org/10.1128/MCB.25.24.10875-10894.2005

Wang, W., J. Huang, X. Wang, J. Yuan, X. Li, L. Feng, J.I. Park, and J. Chen. 2012. PTPN14 is required for the density-dependent control of YAP1. *Genes Dev.* 26:1959–1971. https://doi.org/10.1101/gad.192955.112

Wong, P.G., S.L. Winter, E. Zaika, T.V. Cao, U. Oguz, J.M. Koomen, J.L. Hamlin, and M.G. Alexandrow. 2011. Cdc45 limits replicon usage from a low density of preRCs in mammalian cells. *PLoS One*. 6:e17533. https://doi.org/10.1371/journal.pone.0017533

Zhou, H.J., J. Wang, B. Yao, S. Wong, S. Djakovic, B. Kumar, J. Rice, E. Valle, F. Soriano, M.K. Menon, et al. 2015. Discovery of a First-in-Class, Potent, Selective, and Orally Bioavailable Inhibitor of the p97 AAA ATPase (CB-5083). *J. Med. Chem.* 58:9480–9497. https://doi.org/10.1021/acs.jmedchem.5b01346

Supplemental material

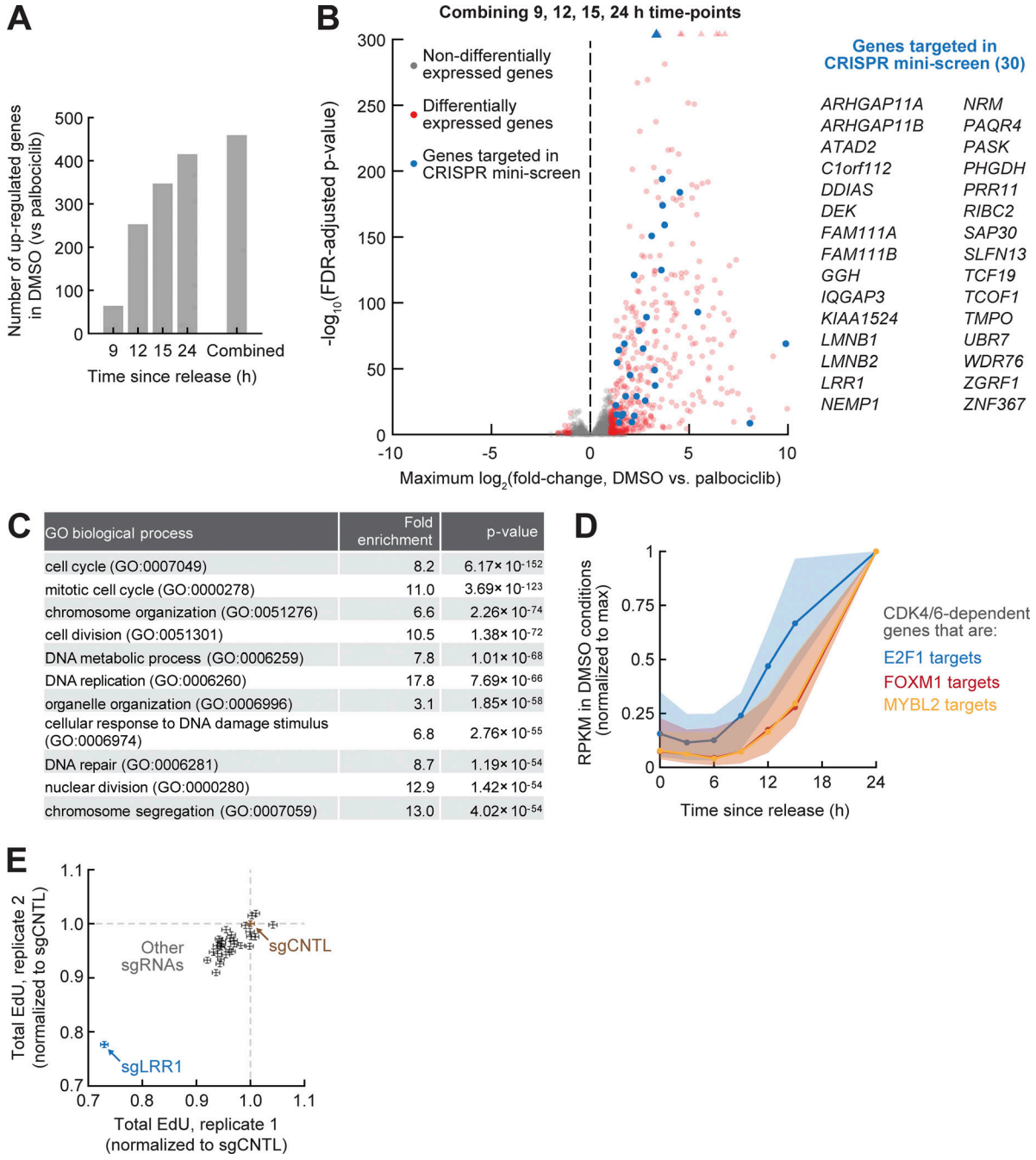

Figure S1. **RNA-Seq analysis of CDK4/6 activity-regulated genes in MCF10A cells (related to Fig. 1). (A)** Number of up-regulated genes in DMSO-treated cells compared with palbociclib treatment (log_2[fold-change] > 1, adjusted P value < 0.1). **(B)** Volcano plot from differential expression analysis. Differentially expressed genes (|log_2[fold-change]| > 1, adjusted P value < 0.1 at any time point) are highlighted in red. Genes targeted in CRISPR screen are highlighted in blue. Triangles indicate genes that lie outside the maximum y-axis range. **(C)** GO term analysis of CDK4/6–dependent genes. Processes are sorted by false discovery rate (FDR)–adjusted P value. Redundant processes are omitted. **(D)** Gene expression time course for CDK4/6–dependent genes that are also E2F1, FOXM1, or MYBL2 targets. For each gene, average expression of DMSO-treated cells at each time point was normalized to maximum expression of that gene. Line plots are medians of genes; shaded error bars indicate 25th to 75th percentile (n = 208, 150, and 142 targets for E2F1, FOXM1, and MYBL2, respectively; n = 3 independent experiments). **(E)** Same experiment as Fig. 1 H. Rate of EdU incorporation was measured in S-phase cells as the total EdU fluorescence in the nucleus and normalized to control cells (sgCNTL). Error bars are population medians with 95% confidence intervals ($n \geq 8{,}725$ cells per condition). RPKM, reads per kilobase of transcript per million mapped reads.

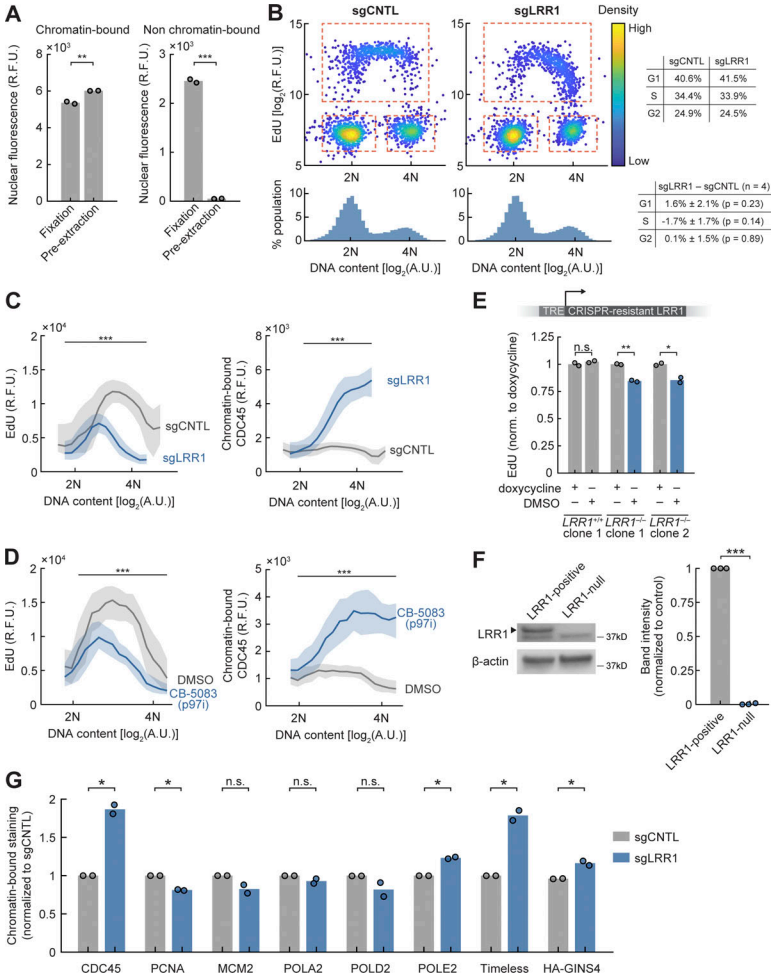

Figure S2. **Analysis of replisome disassembly and DNA replication after LRR1 loss (related to Fig. 2). (A)** Nuclear abundance of chromatin-bound (histone H2B-mTurquoise) and nonchromatin-bound (hDHB-mVenus; see Fig. S5 C) fluorescent proteins in cells that were directly fixed and in cells that were preextracted before fixation. Two-sample Student's *t* test; P = 8.8 × 10^{-3}, 2.2 × 10^{-4} (*n* = 2 technical replicates, *n* ≥ 14,386 cells per replicate). **(B)** Cell-cycle progression in asynchronously cycling cells that were transfected with sgRNAs and fixed 1 d later. Left: G1/S/G2 gating using EdU-DNA content scatter plot (*n* = 2,000 random cells displayed) and distribution of DNA content (*n* ≥ 20,625 cells per condition). Top right: quantification of G1/S/G2 gating from scatter plot. Bottom right: quantification of G1/S/G2 gating in *n* = 4 independent experiments, shown as mean ± SD. P values are from paired Student's *t* tests (*n* ≥ 19,134 cells per condition). To reconcile the fact that (i) percentages of G1/S/G2 cells are not significantly different between control and LRR1 knockout cells and (ii) there is indeed G2 arrest in these cells (lower percentage of cells that are going into mitosis, as shown in Fig. 4), note that these scatter plots are from cells fixed 1 d after LRR1 knockout, and this is likely the first cell cycle that the cells went through in the absence of LRR1 protein. As a result, the G2 arrest is only beginning to manifest and is not captured by a higher percentage of G2 cells. **(C)** RPE-1 hTERT cells stably expressing Cas9 were transfected with sgRNAs and fixed 1 d later. Left: Rate of EdU incorporation in S-phase cells as a function of DNA content. Right: Abundance of chromatin-bound CDC45 in S-phase cells as a function of DNA content. Line plots are population medians in each bin; shaded error bars indicate 25th to 75th percentile (*n* ≥ 68 cells per bin, *n* = 36,413 and 19,133 cells total). Two-sample Student's *t* test; ***, P < 1 × 10^{-3}. Data are representative of two technical replicates. **(D)** Cells were treated with a p97 inhibitor (CB-5083, 4 µM) for 2 h and fixed. Left: Rate of EdU incorporation in S-phase cells as a function of DNA content. Right: Abundance of chromatin-bound CDC45 in S-phase cells as a function of DNA content. Line plots are population medians in each bin; shaded error bars indicate 25th to 75th percentile (*n* ≥ 78 cells per bin, *n* = 3,985 and 4,507 cells total). Two-sample Student's *t* test; ***, P < 1 × 10^{-3}. Data are representative of two independent experiments. **(E)** Cells expressing CRISPR-resistant LRR1 from a doxycycline-inducible promoter were transfected with sgCNTL or sgLRR1 and selected for stable single-cell clones. Cells were cultured in doxycycline to maintain expression of exogenous LRR1. Rate of EdU incorporation was measured in S-phase cells after replacing doxycycline with DMSO or doxycycline for 1 d. Two-sample Student's *t* test; P = 0.29, 3.0 × 10^{-3}, 0.030 (*n* = 2 technical replicates, *n* ≥ 1,436 cells per replicate). The reduction in DNA replication rate was mild after the removal of doxycycline, possibly due to incomplete transcriptional shutdown from the doxycycline-inducible promoter. To further deplete LRR1, *LRR1*$^{-/-}$ cells expressing exogenous LRR1 were transfected with LRR1-targeting siRNA along with doxycycline removal, which achieved near complete (~97%) depletion of LRR1 protein (Fig. S2 F) and a large reduction in DNA replication rate and failure to unload CMG helicases from chromatin in S-phase cells (Fig. 2 G, middle and bottom). **(F)** LRR1 was depleted in *LRR1*$^{-/-}$ cells expressing exogenous, doxycycline-inducible LRR1 by removing doxycycline and transfecting siRNA targeting exogenous LRR1 1 d before fixation. As a negative control, the same cell line was treated with doxycycline and nontargeting siRNA. Cells were harvested and blotted for LRR1. Arrowhead indicates LRR1-specific band; the other band is a nonspecific band. Right: Quantification of Western blots (relative to actin loading control) normalized to control. Paired Student's *t* test; P = 8.3 × 10^{-6} (*n* = 3 independent experiments). **(G)** Abundance of chromatin-bound replisome components in S-phase cells normalized to control cells. Higher levels of CDC45, POLE2, Timeless, and HA-GINS4 were detected in LRR1 knockout cells. Paired Student's *t* test; P = 0.032, 0.024, 0.21, 0.27, 0.31, 0.028, 0.040, 0.020 (*n* = 2 independent experiments, *n* ≥ 3,931 cells per condition; HA-GINS4: *n* = 2 technical replicates, *n* ≥ 3,552 cells per replicate). A.U., arbitrary unit; norm., normalized; R.F.U., relative fluorescence unit; TRE, tetracycline-responsive element. In all panels, *, P < 0.05; **, P < 0.01; ***, P < 0.001.

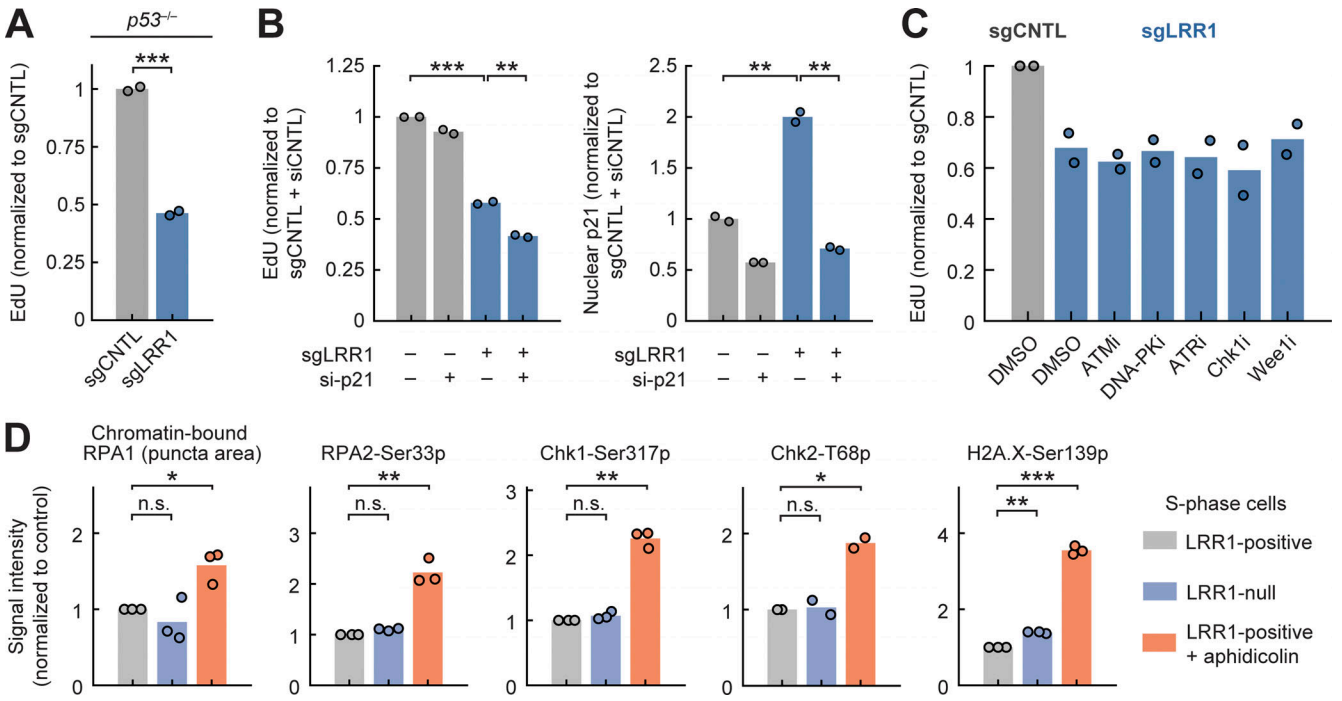

Figure S3. **Suppression of DNA replication after LRR1 loss is not due to DNA damage signaling (related to Fig. 3). (A)** Effect of LRR1 knockout was measured in p53$^{-/-}$ cells. Rate of EdU incorporation in S-phase cells was normalized to control cells. Two-sample Student's *t* test; P = 6.0 × 10^{-4} (*n* = 2 technical replicates, *n* ≥ 1,864 cells per replicate). Data are representative of two independent experiments. **(B)** Serum-starved cells stably expressing Cas9 were transfected with sgRNAs, released from starvation 2 d later, and fixed after 30 h. Left: Rate of EdU incorporation in S-phase cells normalized to control cells (sgCNTL + siCNTL). Two-sample Student's *t* test; P = 1.8 × 10^{-4}, 2.4 × 10^{-3} (*n* = 2 technical replicates, *n* ≥ 1,904 cells per replicate). Right: Nuclear abundance of p21 in S-phase cells normalized to control cells. Two-sample Student's *t* test; P = 3.2 × 10^{-3}, 1.7 × 10^{-3} (*n* = 2 technical replicates, *n* ≥ 1,904 cells per replicate). It was previously reported that CRL2^{LRR1} targets the CDK inhibitor p21 for degradation (Starostina et al., 2010). While LRR1 knockout resulted in higher levels of nuclear p21 in S phase, knockdown of p21 did not rescue the DNA replication defect after LRR1 knockout. **(C)** Rate of EdU incorporation in S-phase cells after 4-h treatment with ATM inhibitor (ATMi; KU-60019, 5 µM), DNA-PK inhibitor (DNA-PKi; NU7441, 1 µM), ATR inhibitor (ATRi; AZ20, 1 µM), Chk1 inhibitor (Chk1i; CHIR124, 500 nM), or Wee1 inhibitor (Wee1i; MK1775, 1 µM) and normalized to control cells (*n* ≥ 2,909 cells per condition). Data from *n* = 2 independent experiments. **(D)** LRR1 was depleted in *LRR1*$^{-/-}$ cells expressing exogenous, doxycycline-inducible LRR1 by removing doxycycline and transfecting siRNA targeting exogenous LRR1 1 d before fixation. As a negative control, the same cell line was treated with doxycycline and nontargeting siRNA. As a positive control, cells were treated with 10 µM aphidicolin for 3 h. The indicated protein markers were measured in S-phase cells through immunofluorescence, and nuclear signals were normalized to control cells (LRR1 positive). Paired Student's *t* test; *, P < 0.05; **, P < 0.01; ***, P < 0.001 (*n* = 3 independent experiments, *n* ≥ 959 cells per condition). The lack of increase in damage signal was not due to measurement insensitivity, as positive control cells treated with the DNA polymerase inhibitor aphidicolin showed elevated signals, and more importantly, elevated signals were also detected when these LRR1-null cells progressed into G2 phase (Fig. 4 I). In all panels, *, P < 0.05; **, P < 0.01; ***, P < 0.001.

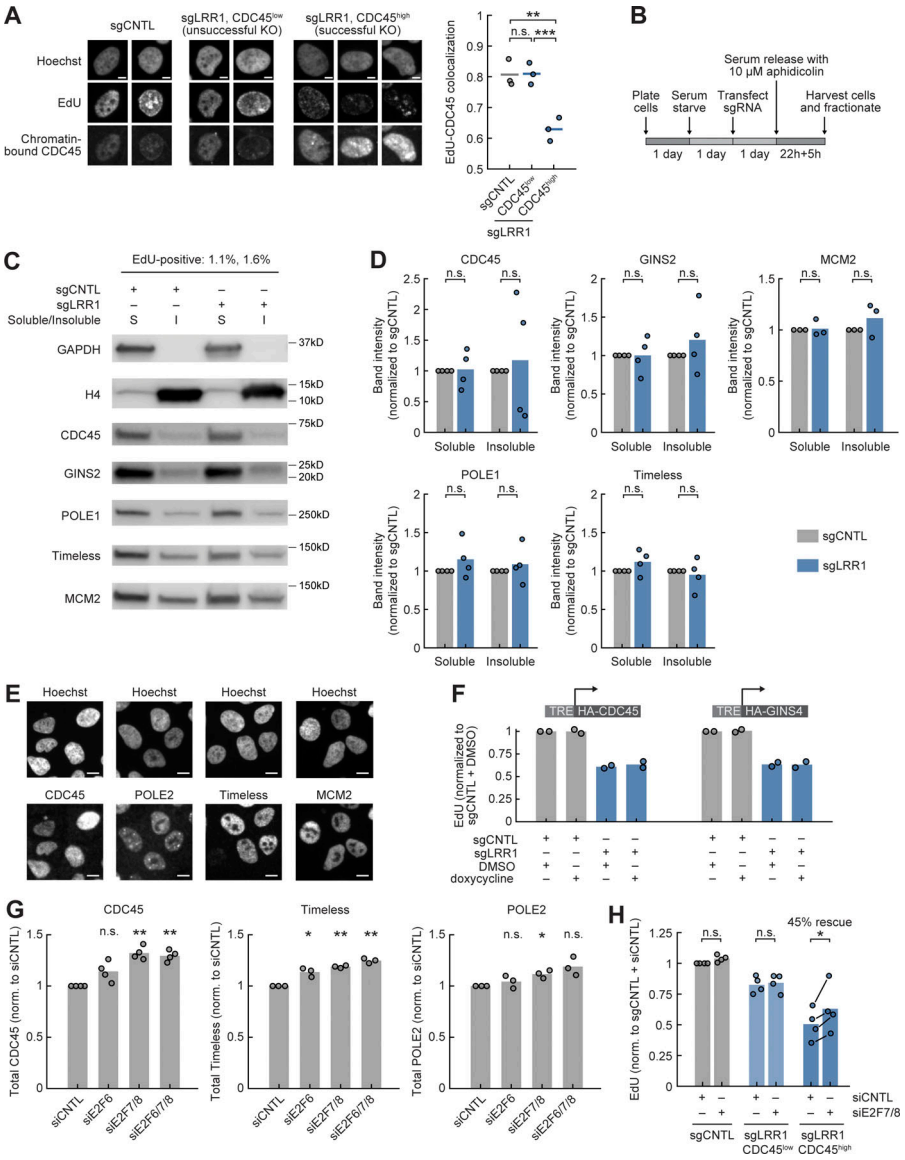

Figure S4. **Control experiments supporting the defective recycling model (related to Fig. 3). (A)** Left: Sample immunofluorescence images of S-phase cells. In sgCNTL and sgLRR1 (CDC45^{low}) cells, EdU and CDC45 stains were largely colocalized, whereas the stains were less colocalized in sgLRR1 (CDC45^{high}) cells. Scale bar: 5 µm. Right: Colocalization of EdU and CDC45 stains was quantified in each nucleus using pixel-level Pearson's correlation coefficient. Paired Student's *t* test; sgCNTL vs. sgLRR1 (CDC45^{low}): P = 0.81; sgLRR1 (CDC45^{low}) vs. sgLRR1 (CDC45^{high}): P = 1.2 × 10^{-4}; sgCNTL vs. sgLRR1 (CDC45^{high}): P = 3.5 × 10^{-3} (*n* = 3 independent experiments, *n* ≥ 1,230 cells per condition). **(B)** Schematic of experimental setup for subcellular fractionation (control experiment for Fig. 3, B–D). Serum-starved cells stably expressing Cas9 were transfected with sgRNAs and released from starvation in the presence of 10 µM aphidicolin to synchronize cells at the G1/S transition. **(C)** Control and LRR1 knockout cells were not released from an aphidicolin block and harvested. Detergent-soluble (S) and insoluble (I) proteins were fractionated and immunoblotted. Soluble and insoluble fractions were loaded at a ratio of 1:2. Data are representative of four independent experiments. **(D)** Quantification of C and replicates (relative to GAPDH or H4 loading controls) normalized to control cells. Paired Student's *t* test; CDC45: P = 0.95, 0.70; GINS2: P = 0.87, 0.50; POLE1: P = 0.31, 0.60; Timeless: P = 0.25, 0.59; MCM2: P = 0.84, 0.38 (*n* = 4 independent experiments). **(E)** Subcellular localization of total CDC45, POLE2, Timeless, and MCM2 measured by immunofluorescence. Scale bar: 10 µm. Data are representative of three independent experiments. CDC45, POLE2, Timeless, and MCM2 were all exclusively nuclear localized, suggesting that the detergent-soluble fraction of these replisome components reflects the nucleoplasmic pool rather than the cytoplasmic pool. **(F)** Rate of EdU incorporation in S-phase cells was normalized to control cells (*n* ≥ 25,192 cells per condition). Data from *n* = 2 independent experiments. Expressing exogenous CDC45 or GINS4 alone did not rescue the DNA replication defect after LRR1 knockout. This result suggests that additional rate-limiting components or a combination of rate-limiting components is sequestered on chromatin, which is consistent with subcellular fractionation results where multiple replication factors were depleted from the soluble pool (Fig. 3 D). This led us to rescue DNA replication defects in LRR1 knockout cells by de-repressing E2F activity (Fig. 3 G). **(G)** Total nuclear levels of CDC45, Timeless, and POLE2 were measured in S-phase cells and normalized to control cells. Paired Student's *t* test; CDC45: P = 0.057, 1.4 × 10^{-3}, 1.2 × 10^{-3} (*n* = 4 independent experiments, *n* ≥ 9,916 cells per condition); Timeless: P = 0.029, 1.3 × 10^{-3}, 2.4 × 10^{-3} (*n* = 3 independent experiments, *n* ≥ 10,680 cells per condition); POLE2: P = 0.356, 0.032, 0.060 (*n* = 3 independent experiments, *n* ≥ 2,532 cells per condition). **(H)** Rate of EdU incorporation in S-phase cells normalized to control cells (sgCNTL + siCNTL). Cells were categorized as CDC45^{low} (unsuccessful knockout) or CDC45^{high} (successful knockout) based on the abundance of chromatin-bound CDC45. Paired Student's *t* test; P = 0.069, 0.31, 0.015 (*n* = 4 independent experiments, *n* ≥ 164 cells per condition). KO, knockout; norm., normalized; TRE, tetracycline-responsive element. In all panels, *, P < 0.05; **, P < 0.01; ***, P < 0.001.

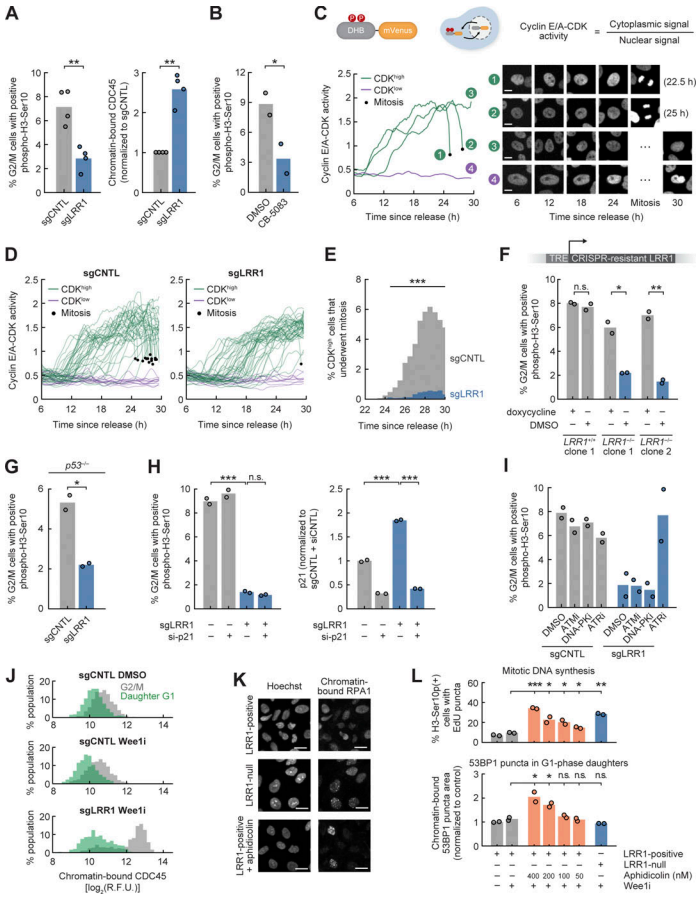

Figure S5. **Analysis of the G2/M checkpoint and under-replicated DNA after LRR1 loss (related to Fig. 4). (A)** Continuously cycling cells stably expressing Cas9 were transfected with sgRNAs and fixed 1 d later. Left: Percentage of G2/M cells with positive phospho-H3-Ser10 signal. Paired Student's *t* test; P = 3.3 × 10^{-3} (*n* = 4 independent experiments, *n* ≥ 3,421 cells per condition). Right: Abundance of chromatin-bound CDC45 in G2/M-phase cells normalized to control cells. Paired Student's *t* test; P = 1.3 × 10^{-3} (*n* = 4 independent experiments, *n* ≥ 3,421 cells per condition). **(B)** Cells were treated with DMSO or a p97 inhibitor (CB-5083, 4 µM) for 6 h. Percentage of G2/M cells with positive phospho-H3-Ser10 signal. Paired Student's *t* test; P = 0.044 (*n* = 2 independent experiments, *n* ≥ 3,522 cells per condition). **(C)** Top: Schematic of cyclin E/A–CDK activity reporter. DHB is a fragment (aa 994–1087) of the human DHB protein. The reporter translocates to the cytoplasm when phosphorylated by cyclin E/A–CDK activity. Bottom: Cells expressing H2B-mTurquoise and the cyclin E/A–CDK activity reporter were released from serum starvation and imaged and further categorized as CDK-high if cyclin E/A–CDK activity rose above 0.85 for more than 1 h. Mitosis was monitored by the separation of condensed chromatin during anaphase (see bottom right sample images). Cells #1 and #2 underwent mitosis at 22.5 h and 25 h after release, respectively. Cells #3 and #4 did not undergo mitosis within 30 h after release. Scale bar: 10 µm. **(D)** Serum-starved cells stably expressing Cas9 were transfected with sgRNAs and released from starvation 2 d later. Cyclin E/A–CDK activity and mitotic time were measured (*n* = 50 sample traces displayed). Data are representative of three independent experiments. **(E)** Quantification of D. Percentage of CDK^{high} cells that underwent mitosis is plotted as a function of time since serum release (*n* = 6,016 and 5,979 cells). Fisher's exact test; ***, P < 1 × 10^{-3}. Data are representative of three independent experiments. **(F)** Cells expressing CRISPR-resistant LRR1 from a doxycycline-inducible promoter were transfected with sgCNTL or sgLRR1 and selected for stable single-cell clones. Cells were cultured in doxycycline to maintain expression of exogenous LRR1. Percentage of G2/M cells with positive phospho-H3-Ser10 signal was measured after replacing doxycycline with DMSO or doxycycline for 1 d. Two-sample Student's *t* test; P = 0.38, 0.016, 3.7 × 10^{-3} (*n* = 2 technical replicates, *n* ≥ 2,104 cells per replicate). **(G)** Effect of LRR1 knockout was measured in $p53^{-/-}$ cells. Percentage of G2/M cells with positive phospho-H3-Ser10 signal. Two-sample Student's *t* test; P = 0.014 (*n* = 2 technical replicates, *n* ≥ 4,111 cells per replicate). **(H)** Serum-starved cells stably expressing Cas9 were transfected with sgRNAs, released from starvation 2 d later, and fixed after 30 h. Left: Percentage of G2/M cells with positive phospho-H3-Ser10 signal. Two-sample Student's *t* test; P = 1.1 × 10^{-3}, 0.11 (*n* = 2 technical replicates, *n* ≥ 5,807 cells per replicate). Right: Nuclear abundance of p21 in G2/M cells normalized to control cells (sgCNTL + siCNTL). Two-sample Student's *t* test; P = 8.7 × 10^{-4}, 1.0 × 10^{-4} (*n* = 2 technical replicates, *n* ≥ 5,807 cells per replicate). **(I)** Percentage of G2/M cells with positive phospho-H3-Ser10 signal after 4-h treatment with ATM inhibitor (ATMi; KU-60019, 5 µM), DNA-PK inhibitor (DNA-PKi; NU7441, 1 µM), or ATR inhibitor (ATRi; AZ20, 1 µM; *n* ≥ 4,648 cells per condition). Data from two independent experiments. **(J)** Histogram of chromatin-bound CDC45 in G1-phase daughter cells or G2/M cells after 4-h treatment with DMSO or Wee1 inhibitor (Wee1i; MK1775, 1 µM; *n* ≥ 356 cells per condition). Data are representative of two technical replicates. **(K)** Sample immunofluorescence images from experiment in Fig. 4 I. Scale bar: 20 µm. Data are representative of three independent experiments. **(L)** LRR1 was depleted in *LRR1*$^{-/-}$ cells expressing exogenous, doxycycline-inducible LRR1 by removing doxycycline and transfecting siRNA targeting exogenous LRR1 1 d before fixation. As a positive control, cells were treated with the indicated concentration of aphidicolin for 16 h. Top: Cells were treated with Wee1 inhibitor (MK1775, 1 µM) for 1 h and pulse labeled with EdU for 10 min. EdU puncta area was quantified in mitotic cells with positive phospho-H3-Ser10 signal. Two-sample Student's *t* test; P = 7.2 × 10^{-4}, 0.047, 0.038, 0.025, 1.5 × 10^{-3} (*n* = 2 technical replicates, *n* ≥ 209 cells per condition). Bottom: Cells were treated with Wee1 inhibitor (MK1775, 1 µM) for 3 h, and chromatin-bound 53BP1 puncta area was quantified in G1-phase daughter cells born after Wee1 inhibition. Two-sample Student's *t* test; P = 0.0498, 0.030, 0.32, 0.77, 0.090 (*n* = 2 technical replicates, *n* ≥ 582 cells per condition). R.F.U., relative fluorescence unit; TRE, tetracycline-responsive element. In all panels, *, P < 0.05; **, P < 0.01; ***, P < 0.001.

Provided online are five Excel tables. Table S1 shows raw RNA-Seq read counts for all genes and samples. Table S2 presents results from differential expression analysis of RNA-Seq experiments. Table S3 lists CDK4/6 activity-dependent genes and their manually annotated function. Table S4 lists target genes of E2F1, FOXM1, and MYBL2 identified from an analysis of publicly available ChIP-Seq results (ENCODE). Table S5 provides sequences of crRNAs and siRNAs used in this study.